

## Research paper

## A phase-change approach to landslide simulations: Coupling finite strain elastoplastic TLSPH with non-Newtonian IISPH

Daniel S. Morikawa <sup>a,\*</sup>, Mitsuteru Asai <sup>b</sup><sup>a</sup> JAMSTEC, Center for Mathematical Science and Advanced Technology, Zip code: 236-0001, 3173-25, Showa-machi, Kanazawa-ku, Yokohama-city, Kanagawa, Japan<sup>b</sup> Kyushu University, Department of Civil and Structural Engineering, Zip code: 819-0395, 744 Motooka Nishi-ku, Fukuoka, Japan

## ARTICLE INFO

## Keywords:

Landslide  
Slope stability  
Smoothed particles hydrodynamics  
Total Lagrangian  
Non-Newtonian fluids  
Phase-change

## ABSTRACT

The present work shows a novel phase-change concept for simulating landslides using the smoothed particles hydrodynamics (SPH) method. The idea is to initiate the simulation of a slope stability problem with a Solid Mechanics-based SPH, modeling the soil as an elastoplastic material at finite strain. Next, if a particle exceeds a certain level of plastic strain, such particle changes its phase to a fluid state with non-Newtonian rheology, which is then solved with a Fluid Dynamics-based SPH method. We use the total Lagrangian SPH (TLSPH) method to solve the Solid Mechanics phase to avoid problems related to particle distribution (such as the tensile instability), while the implicit incompressible SPH (IISPH) to solve the Fluid Dynamics part to avoid the restriction on time increment in relation to high values of viscosity. The coupling between the two phases is treated as a conventional fluid–solid interaction (FSI) problem. We verified the proposed TLSPH method with the triaxial compression problem and demonstrated the robustness of the proposed phase-change TLSPH–IISPH coupled method in the simulation of the Aso landslide. Specifically, it may be the first time to simulate the Aso landslide from its initiation to its propagation in a single numerical simulation.

## 1. Introduction

Landslide is a generic term to refer to any type of rapid mass movement (Montgomery, 2014). As reviewed by Terzaghi (1950), landslides may be initiated by several mechanisms classified either as external (e.g., earthquakes, heavy rain, etc.) or internal (e.g., changes in the material strength). Traditionally, landslide initiation has been evaluated by slope stability methods such as the Culmann's finite-slope stability model (Culmann, 1875) and the Bishop's simplified method of slices (Bishop, 1955). However, such methods require to define a specific slip surface in advance to check its stability, and, due to its simplicity, many landslide scenarios might not be well defined by such methods. Furthermore, this class of methods do not support any attempt in assessing the post-failure behavior of the landslide.

Given the recent advances in computer technology, several researchers have attempted to simulate the landslide phenomena using numerical methods. One common approach is to use the distinct element method (DEM) and the discontinuous deformation analysis (DDA) in combination with other methods (usually a computational fluid dynamics solver). Examples for DEM might include Tsuji et al. (2007), Kumar et al. (2012), An et al. (2022), and for DDA, Wang et al. (2016a,b, 2017, 2019), Peng et al. (2019). However, DEM and DDA

are based on physical grain dynamics, which means that it requires an extremely large amount of computational power to reproduce the desired phenomena.

In contrast, there are several continuum-based methods used in landslide simulations, in which the soil skeleton is modeled according to its macroscopic behavior. Here, we highlight the finite element method (FEM) (Cascini et al., 2010, 2013; Laloui et al., 2013), and the material point method (MPM) (Beuth et al., 2008, 2010; Bandara and Soga, 2015; Liang et al., 2022) as two examples of greatly well-known methods. A great review on continuum-based numerical methods can be found in Soga et al. (2015). Among these continuum-based methods, we selected the smoothed particle hydrodynamics (SPH) for the development of our proposed phase-change method.

Proposed by Gingold and Monaghan (1977) and Lucy (1977), the SPH method is a Lagrangian mesh-less method initially developed for Astrophysics problems and later expanded to Fluid Dynamics (eg., Monaghan (1992), Morris et al. (1997), Violeau and Issa (2007), Asai et al. (2012)), Solid Mechanics (eg. Libersky and Petschek (1990), Stellingwerf and Wingate (1993), Gray et al. (2001), Lee et al. (2016)), fluid–structure interaction (eg., Antoci et al. (2007), Khayyer et al. (2018), Morikawa and Asai (2021)), among others.

\* Corresponding author.

E-mail address: [morikawad@jamstec.go.jp](mailto:morikawad@jamstec.go.jp) (D.S. Morikawa).

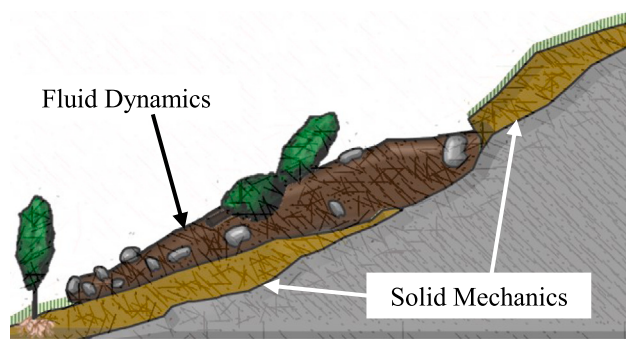


**Fig. 1.** Concept of the proposed multi-physics method for simulating landslides.

Recently, SPH has received significant attention in the simulation of Geomechanics problems, including landslides. In the authors' opinion, most published works can be divided into two classifications: treating the soil with Solid Mechanics (either as an elastic or elastoplastic material) and treating the soil with Fluid Dynamics.

In the first group we may include Maeda et al. (2004) (later translated to English in Maeda et al. (2006)) as probably the first attempt of SPH usage for Geomechanics, Bui and Fukagawa (2009) and Blanc and Pastor (2012) with their expansion to solve the  $\mathbf{u}$ - $p$  set of equations (Zienkiewicz et al., 1999), Bui and Nguyen (2017) for solving the complete soil–water coupling problem in a two phases–two points manner, and Morikawa and Asai (2022) for solving the  $\mathbf{u}$ - $\mathbf{w}$ - $p$  set of equations (Biot, 1956; Zienkiewicz et al., 1999) in a two phases–one point scheme, among others.

In the second group, the earliest work that we are aware of is from McDougall and Hung (2004), where they combined the SPH method with depth-integration equations to simulate the landslide propagation problem, followed by Pastor et al. (2009) in a similar fashion. Other works might include (but not limited by) Naili and Matsushima (2005), who implemented and SPH method with non-Newtonian rheology for liquefaction problems, Cascini et al. (2014), Dai et al. (2016), Pastor et al. (2015), Han et al. (2019), who used SPH to simulate large scale landslides.

The advantage of simulating Geomechanics problems in the context of Solid Mechanics is that it is possible to include a variety of concepts from Geotechnical Engineering such as soil–water coupling, effective stress, drained and undrained conditions, etc. On the other hand, it was pointed out in Dai et al. (2016) that the elastoplastic constitutive model constructed in the framework of Solid Mechanics is not physically consistent above a certain amount of deformation such as in debris flow. Hence, it may be necessary to use Fluid Dynamics to simulate extremely large deformed problems with SPH. However, a shortcoming of this approach is the impossibility of evaluating the initiation of the landslide, in other words, one must define beforehand the slip surface to start the simulation. In summary, the simulation of both initiation and propagation is very difficult since the two phases of the landslide are usually modeled with two different physical constitutive models. This, along with other difficulties which are beyond the scope of this work (such as retrieving physical characteristics of the soil given its spatial variation and large scale, etc.), makes landslide simulation an exceptionally challenging problem.

The current work innovates in bringing the concept of phase-change for the simulation of landslides from initiation to post-failure, as illustrated in Fig. 1. The idea is to combine the two frameworks mentioned above in a single method; that is, simulating the stable part of the soil with Solid Mechanics and, once it reaches a certain level of plastic deformation, transform its phase into a fluidized material. Then, the landslide propagation follows with the simulation of such fluidized material with Fluid Dynamics. Hence, we developed a method capable

of simulating both landslide initiation and post-failure behavior at extremely large strains.

One alternative idea is to simulate the slope stability problem with an interface solver and later simulate the landslide propagation with SPH (Lin et al., 2019). However, our proposed phase-change method is intrinsically more comprehensive in the sense that it is not necessary to define a slip surface at the beginning of the simulation. Furthermore, other researchers proposed to model the post-failure with the introduction of discontinuities with the extended FEM (Sanborn and Prévost, 2011; Salimzadeh and Khalili, 2015) and its modification to the Material Point Method (Liang et al., 2022). As a drawback, this approach requires two additional computations. First, the determination of the landslide soil detachment as the initiation of the discontinuity. Then, the solution of a self-contact problem with friction between the detached soil and the original soil mass. In comparison, our proposed method is relatively easier, since an explicit expression to calculate the initiation of the discontinuity is not necessary. In addition, we consider that our proposed method is more appropriate for extremely high strain problems such as debris flow events.

To achieve the desirable accuracy, we chose a Total Lagrangian (TL) framework to model the Solid Mechanics part (as in Lee et al. (2016), Morikawa and Asai (2021)). TL formulations are well-known to increase the accuracy of Solid Mechanics-based SPH methods, given that particle distribution is unchanged throughout the simulation. This fact solves the tensile instability, one of the most significant shortcomings of SPH. In addition, we adapted a finite strain elastoplastic stress update based on the logarithmic strain presented in de Souza Neto et al. (2008) to the TLSRH framework.

For the Fluid Dynamics part, we use the implicit incompressible SPH method (IISPH) as presented in Morikawa et al. (2019) to avoid constraints in time increment in relation to the value of viscosity. The implicit formulation is crucial since we model the rheology of the landslide as a non-Newtonian fluid, which might result in arbitrarily high viscosity. Finally, the coupling mechanism between TLSRH and IISPH is solved as an FSI problem, similar to the one presented in Morikawa and Asai (2021).

## 2. The SPH method

This study is based on the SPH method as the spatial discretization method for all equations. Readers interested in understanding the derivations of the SPH approximations used throughout the article should refer to classical studies such Monaghan (1992), Randles and Libersky (1996), Bonet and Lok (1999), Ganzenmüller (2015).

We start expressing the original SPH approximation of a generic function  $f$  as

$$\langle f \rangle_i = \sum_j \frac{m_j}{\rho_j} f_j W(\mathbf{r}_{ij}, h), \quad (1)$$

where  $i$  and  $j$  stands for target and a neighbor particles, respectively,  $m$  the mass,  $\rho$  the density,  $\mathbf{r}_{ij} = \mathbf{x}_i - \mathbf{x}_j$  the relative position vector,  $W$  the weight function (also called kernel) and  $h$  the smoothing length. In this study, we selected the cubic spline kernel (Schoenberg, 1964) with smoothing length  $h = 1.2d$ , where  $d$  is the particle diameter.

In practice, the spatial derivatives in the SPH are derived from the derivative of the kernel  $\nabla W$ , where  $\nabla$  is the nabla operator. One might use a different form of the SPH spatial derivative for each variable. For example, the traditional equations (Monaghan, 1992) using  $\nabla W$  have been proved to be highly stable for Fluid Dynamics problems but lack the necessary accuracy in some cases. On the other hand, the corrected forms using  $\tilde{\nabla}W$  (Randles and Libersky, 1996; Bonet and Lok, 1999; Ganzenmüller, 2015) improve their accuracy with the shortcoming of being more sensitive to uneven particle distributions.

In this study, we chose the corrected forms of the kernel gradient  $\tilde{\nabla}W$  for the solid phase (Randles and Libersky, 1996; Bonet and Lok, 1999; Ganzenmüller, 2015), while using the traditional kernel gradient

$VW$  (Monaghan, 1992) for the fluid phase. The reason for that is, from personal experience, the total Lagrangian scheme in the solid phase provides extended stability for the method, while the highly dynamic nature of the fluid phase results in high demands for numerical stability. We provide the SPH approximation form used in each governing equation in the following sections.

### 3. Solid phase: finite strain elastoplastic TLSPH

Although the original SPH is referred to as a Lagrangian particle method, it still has some Eulerian nature because the interaction neighbor particles are redefined for every current particle position within a fixed influence radius. As a result, the tensile instability encountered in SPH is caused by such Eulerian kernel functions (Belytschko et al., 2000a). The TLSPH follows the total Lagrangian description of kinematics, in which the reference configuration is fixed its initial undeformed configuration of particles. The TLSPH can solve not only large deformed elastic bodies but also elastoplastic bodies as long as its topology does not change. In this section, the TLSPH for the elastoplastic material is summarized and slightly extended to geomaterial applications. To this end, we introduce a simple update formula for the porosity and a phase-change limit to refer to the total accumulated plastic strain.

#### 3.1. Governing equations

The conservation of linear momentum for the total Lagrangian description can be written as

$$\frac{D\mathbf{v}}{Dt} = \frac{1}{\rho_0} \nabla_0 \cdot \mathbf{P} + \mathbf{g}, \quad (2)$$

where  $\mathbf{g}$  is the external acceleration vector,  $\nabla_0 = (\frac{\partial}{\partial X}, \frac{\partial}{\partial Y}, \frac{\partial}{\partial Z})^T$  is the material nabla operator (i.e., in relation to the reference configuration  $\mathbf{X}$ ),  $\rho$  the density,  $\mathbf{P}$  the nominal stress,<sup>1</sup> and the subscript 0 the reference (initial) configuration. Notice that, since we are dealing with soil materials,  $\rho_0 = (1 - n_0)\rho_s$ , where  $n$  is the porosity and  $\rho_s$  is the average density of the soil grains.

In Geomechanics problems, it is necessary to update the porosity according to the conservation of mass equation as (Bui and Nguyen, 2017)

$$\frac{Dn}{Dt} = (1 - n)\nabla \cdot \mathbf{v}, \quad (3)$$

which is obtained considering the soil grain density  $\rho_s$  to be incompressible. Notice that the above equation is defined in the current configuration. To adapt to the total Lagrangian scheme, we developed the following equation using the chain rule

$$\frac{Dn}{Dt} = (1 - n)\nabla_0 \mathbf{F}^{-1} \cdot \mathbf{v}, \quad (4)$$

where, already using the SPH approximation and defining  $\beta$  as the current time step, we update it in time as

$$n_i^{\beta+1} = n_i^\beta + \Delta t \frac{1 - n_i^\beta}{\rho_i} \sum_j m_j (\mathbf{v}_j^{\beta+1} - \mathbf{v}_i^{\beta+1}) \cdot \tilde{\nabla} W(\mathbf{R}_{ij}, h) \mathbf{F}_i^{-1}. \quad (5)$$

As usual in total Lagrangian formulations, we calculate the time derivative of the deformation gradient  $\mathbf{F}$  as (de Souza Neto et al., 2008)

$$\frac{D\mathbf{F}}{Dt} = (\nabla_0 \otimes \mathbf{v})^T, \quad (6)$$

where  $T$  is the transpose operator.

<sup>1</sup> Following the nomenclature from Belytschko et al. (2000b) we define  $\mathbf{P}$  as the nominal stress and the first Piola stress as  $\mathbf{P}^T$ .

Updating Eq. (2), (6) and (4) in time, we have

$$\mathbf{v}_i^{\beta+1} = \mathbf{v}_i^\beta + \Delta t \left( \frac{1}{\rho_0} \nabla_0 \cdot \mathbf{P}_i^\beta + \mathbf{g} + \mathbf{C}_{JST,i} \right), \quad (7)$$

and

$$\mathbf{F}^{\beta+1} = \mathbf{F}^\beta + \Delta t (\nabla_0 \otimes \mathbf{v}_i^{\beta+1})^T. \quad (8)$$

Following Lee et al. (2016) and Morikawa and Asai (2021), we define the Jameson–Schmidt–Turkel stabilization (Jameson et al., 1981) term as

$$\mathbf{C}_{JST,i} = c_p d (\epsilon^{(2)} \nabla_0^2 \mathbf{v}_i - d^2 \epsilon^{(4)} \nabla_0^4 \mathbf{v}_i), \quad (9)$$

where  $c_p$  is the p-wave velocity, which, for a solid material with bulk modulus  $K$  and shear modulus  $\mu$ , is defined as

$$c_p = \sqrt{\frac{K + 4\mu/3}{\rho_s}}. \quad (10)$$

In the above equations, the second and fourth derivatives of  $\mathbf{v}$  and the gradient of  $\mathbf{P}$  and  $\mathbf{v}$  are calculated using

$$\langle \nabla^2 \mathbf{v} \rangle_i = \sum_j m_j \frac{8}{\rho_i + \rho_j} \frac{\mathbf{v}_{ij} \cdot \mathbf{r}_{ij}}{\mathbf{r}_{ij}^2} \nabla W(\mathbf{r}_{ij}, h), \quad (11)$$

$$\langle \nabla^4 \mathbf{v} \rangle_i = \sum_j m_j \frac{8}{\rho_i + \rho_j} \frac{\langle \nabla^2 \mathbf{v} \rangle_{ij} \cdot \mathbf{r}_{ij}}{\mathbf{r}_{ij}^2} \nabla W(\mathbf{r}_{ij}, h). \quad (12)$$

$$\langle \nabla_0 \cdot \mathbf{P}^\beta \rangle_i = \rho_i \sum_j m_j \left( \tilde{\nabla} W(\mathbf{R}_{ij}, h) \cdot \frac{\mathbf{P}_i^\beta}{\rho_i^2} - \tilde{\nabla} W(\mathbf{R}_{ji}, h) \cdot \frac{\mathbf{P}_j^\beta}{\rho_j^2} \right), \quad (13)$$

$$\langle \nabla_0 \otimes \mathbf{v}^{\beta+1} \rangle_i^T = \frac{1}{\rho_i} \sum_j m_j (\mathbf{v}_j^{\beta+1} - \mathbf{v}_i^{\beta+1}) \otimes \tilde{\nabla} W(\mathbf{R}_{ij}, h), \quad (14)$$

respectively, where  $\mathbf{R}_{ij} = \mathbf{X}_i - \mathbf{X}_j$  is the relative position vector between particles  $i$  and  $j$  in the reference configuration. Notice that we are dealing with asymmetric tensors, so the order of the multiplications are important. Also, as explained by Lee et al. (2016), the split between two different kernel gradients in Eq. (13) is important when applying the kernel gradient correction to guarantee the conservation of linear momentum.

For the boundary conditions (BC), we apply the same technique as in Morikawa and Asai (2021) for the solid phase. In short, essential BC are trivially enforced as Dirichlet BCs, while natural boundary conditions are derived from the non-penetration condition in addition to Coulomb frictions forces.

#### 3.2. Constitutive model

In this work, we utilize a finite strain elastoplastic constitutive model, where the elastic part follows the Hencky model, while the plastic part might be formulated from any given plastic flow rule and yield condition. The applications for Drucker–Prager and Modified Cam–Clay models are summarized in the Appendix.

##### 3.2.1. Hencky model

The Hencky model is an extension of the linear elastic Hookean law to the finite strain theory based on the logarithmic strain  $\epsilon$ , which is defined as

$$\epsilon = \frac{1}{2} \ln \mathbf{B}, \quad (15)$$

where  $\mathbf{B} = \mathbf{F} \cdot \mathbf{F}^T$  is the left Cauchy–Green strain tensor. Notice that the symbol  $\ln$  in Eq. (15) refers to the tensor logarithmic operation, in contrast with the standard  $\ln$ .

Then, the Kirchhoff stress  $\tau$  follows the same linear stress–strain relationship with  $\epsilon$  as the Cauchy stress with the infinitesimal strain in the standard Hookean material. In mathematical terms,

$$\tau = \mathbf{C}_{el} : \epsilon, \quad (16)$$

where  $\mathbf{C}_{el}$  is the tangent modulus for the Hookean material and the conversion to Cauchy stress is defined as  $\sigma = \tau/J$ .

The use of the logarithmic strain makes an elastoplastic constitutive model at finite strain simple, as demonstrated in the following section.

### 3.2.2. Hyperelastic-plastic return mapping

Usual return mappings are derived from the summation split of the strain tensor ( $\epsilon = \epsilon^e + \epsilon^p$ ). At finite strain, on the other hand, plastic deformation is divided into its elastic and plastic parts according to a multiplicative split of the deformation gradient ( $\mathbf{F} = \mathbf{F}^e \cdot \mathbf{F}^p$ ), which drastically complicates the return mapping.

However, using the Hencky model for the elastic deformation, that is, using the logarithmic strain as explained in Section 3.2.1, we can make the finite strain return mapping to be almost identical to the infinitesimal version. This is easily visualized if one notice that the multiplicative split becomes a summation of logarithms. Mathematically, from the definition of the logarithmic strain (Eq. (15)),

$$\begin{aligned}\epsilon &= \frac{1}{2}(\ln \mathbf{F} \cdot \mathbf{F}^T) \\ &= \frac{1}{2}(\ln(\mathbf{F}^e \cdot \mathbf{F}^p) \cdot (\mathbf{F}^e \cdot \mathbf{F}^p)^T) \\ &= \frac{1}{2}\ln(\mathbf{F}^e \cdot (\mathbf{F}^e)^T) + \frac{1}{2}\ln(\mathbf{F}^p \cdot (\mathbf{F}^p)^T) \\ &= \epsilon^e + \epsilon^p.\end{aligned}\quad (17)$$

In the above equation,  $\epsilon^e$  and  $\epsilon^p$  are the logarithmic elastic and plastic strain tensors, respectively. In this way, the plastic correction can be performed in the same manner as the infinitesimal case as

$$\tau^{\beta+1} = \tau^{\text{trial}} - \Delta\gamma \mathbf{C}_{el} : \mathbf{N}^{\beta+1}, \quad (18)$$

where  $\Delta\gamma$  is the plastic multiplier and  $\mathbf{N}$  is the direction of the plastic flow. The superscript  $\beta+1$  on  $\mathbf{N}$  refers to the fact that  $\mathbf{N}$  is derived from the  $\tau^{\beta+1}$  configuration; therefore, an implicit operation (de Souza Neto et al., 2008).

Eq. (18) works because, in the Hencky model, the Kirchhoff stress has a Hookean relationship with the logarithmic strain (Eq. (16)). In terms of the Cauchy stress, it becomes

$$\sigma^{\beta+1} = \sigma^{\text{trial}} - \Delta\gamma \mathbf{C}_{el}/J : \mathbf{N}^{\beta+1}, \quad (19)$$

where  $J$  is the Jacobian defined as the determinant of  $\mathbf{F}$ .

To define the elastic trial state, we must define the multiplicative update of the deformation gradient as

$$\mathbf{F}^{\beta+1} = \Delta\mathbf{F} \cdot \mathbf{F}^\beta, \quad (20)$$

where,

$$\Delta\mathbf{F} = \mathbf{I} + \Delta t(\nabla_0 \otimes \mathbf{v})^T \cdot (\mathbf{F}^\beta)^{-1}. \quad (21)$$

Considering that we have the logarithmic strain from the previous step, we can retrieve the left Cauchy Green as

$$\mathbf{B}^\beta = 2\exp(\epsilon^\beta), \quad (22)$$

and its update using  $\Delta\mathbf{F}$  defines the elastic trial left Cauchy Green

$$\mathbf{B}^{\text{trial}} = \Delta\mathbf{F} \cdot \mathbf{B}^\beta \cdot \Delta\mathbf{F}. \quad (23)$$

The above equation can be easily derived applying Eq. (20) in the definition of the left Cauchy Green ( $\mathbf{B} = \mathbf{F} \cdot \mathbf{F}^T$ ). Then, the elastic trial logarithmic strain is calculated as

$$\epsilon^{\text{trial}} = \frac{1}{2}\ln\mathbf{B}^{\text{trial}}, \quad (24)$$

and the elastic trial Cauchy stress for the Hencky material as

$$\sigma^{\text{trial}} = \mathbf{C}_{el}/J : \epsilon^{\text{trial}}. \quad (25)$$

Lastly, one must retrieve back the logarithmic strain tensor as

$$\epsilon^{\beta+1} = \frac{1}{E}[(1+\nu)\tau^{\beta+1} - \nu \text{tr}(\tau^{\beta+1})], \quad (26)$$

and the nominal stress as

$$\mathbf{P}^{\beta+1} = (\mathbf{F}^{\beta+1})^{-1} \cdot \tau^{\beta+1}. \quad (27)$$

An algorithmic description of the return mapping for Drucker–Prager and Modified Cam–Clay models are summarized in Appendix A and Appendix B, respectively.

### 3.3. Phase-change

Although a continuous approach might be reasonable for simulating the initiation of a landslide, it is well-known that, in landslides, it occurs a detachment of the landslide soil mass from the main soil slope. To simulate that, we implemented a straightforward yet robust rupture criterion similar to the work of Wang et al. (2021) that can be easily incorporated into our proposed method.

In the case of using Drucker–Prager yield criterion with hardening being applied to the cohesion (as in Appendix A), the main variable to control this hardening behavior is the accumulated plastic strain  $\epsilon_p$ . Our rupture criterion is simply a limitation on  $\epsilon_p$ , that is, particles with  $\epsilon_p$  higher than a threshold  $\epsilon_p^{\text{limit}}$  are labeled “fluidized particles”.

In this case, such fluidized particles stop being treated as solid particles to become fluid particles. Thus, we simply model the phase-change from solid to fluid, and abstain of modeling the reverse fluid to solid phase-change.

## 4. Fluid phase: non-Newtonian IISPH

The solid particles beyond the phase-change limits should no longer be treated as solid but as fluids. The IISPH formulation is applied similarly to Morikawa et al. (2019) to these fluidized particles. In terms of constitutive modeling, we modeled such fluidized particles to follow a Bingham flow non-Newtonian rheology. In other words, the material flows as a fluid at higher stress conditions, while it behaves as a solid-like state below a certain level of stress (called yield stress). Therefore, although we do not model the phase-change from fluid to solid, the settling behavior of the fluidized particles is naturally captured by the Bingham flow non-Newtonian rheology.

### 4.1. Governing equations and projection method

First, let us express the Navier–Stokes and the incompressible conservation of mass equations as follows

$$\frac{D\mathbf{v}}{Dt} = -\frac{1}{\rho}\nabla p + v_f \nabla^2 \mathbf{v} + \mathbf{g}, \quad (28)$$

$$\rho \nabla \cdot \mathbf{v} = 0, \quad (29)$$

where  $v_f$  is the kinematic viscosity. Notice that, as opposed to Eq. (7), this equation is defined in the updated Lagrangian description, that is, the spatial derivatives are defined using the current configuration  $\mathbf{x}$ .

Following the IISPH projection method (Morikawa et al., 2019), the Navier–Stokes equation is split into a predictor and a corrector steps as

$$\mathbf{v}^* = \mathbf{v}^\beta + \Delta t(v_f \nabla^2 \mathbf{v}^* + \mathbf{g}), \quad (30)$$

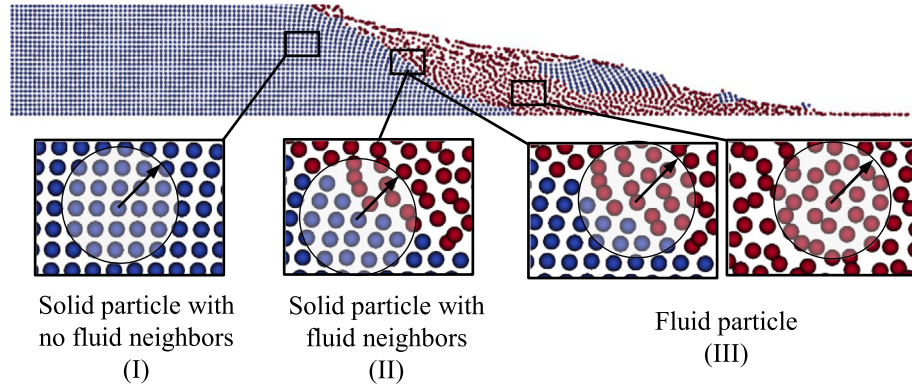


Fig. 2. Schematic illustration of the three different types of particles to deal with in the coupling mechanism.

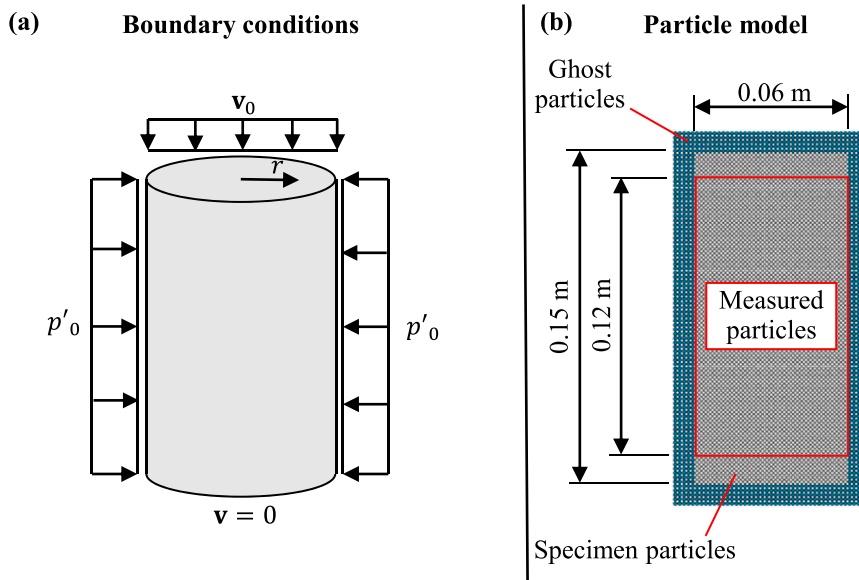


Fig. 3. Triaxial compression test: definition of boundary conditions (a) and its particle model and geometry (b).

$$\mathbf{v}^{\beta+1} = \mathbf{v}^* + \Delta t \left( -\frac{\nabla p^{\beta+1}}{\rho_0} \right), \quad (31)$$

respectively.

For the pressure Poisson equation (PPE), we follow Asai et al. (2012)'s stabilized form, which is obtained by multiplying both sides of Eq. (31) by  $\nabla$  and including a stabilization term. Mathematically, it is expressed as

$$\nabla^2 p^{\beta+1} = \frac{\rho_0 \nabla \cdot \mathbf{v}^*}{\Delta t} + \alpha \frac{\rho_0 - \rho^\beta}{\Delta t^2}. \quad (32)$$

Here,  $\alpha$  is a stabilization parameter in which  $0 \leq \alpha \leq 1$ .

Applying the traditional SPH approximations for the numerical density, viscous term, Laplacian of pressure, divergence of velocity and pressure gradient, we have

$$\langle \rho \rangle_i = \sum_j m_j W(\mathbf{r}_{ij}, h), \quad (33)$$

$$v_f \langle \nabla^2 \mathbf{v} \rangle_i = \sum_j m_j \frac{8(v_{fi} + v_{fj})}{\rho_i + \rho_j} \frac{\mathbf{v}_{ij} \cdot \mathbf{r}_{ij}}{\mathbf{r}_{ij}^2} \nabla W(\mathbf{r}_{ij}, h), \quad (34)$$

$$\langle \nabla^2 p \rangle_i = \frac{2}{\rho_i} \sum_j m_j \frac{\mathbf{r}_{ij} \cdot \nabla W(\mathbf{r}_{ij}, h)}{\mathbf{r}_{ij}^2} (p_i - p_j), \quad (35)$$

$$\langle \nabla \cdot \mathbf{v} \rangle_i = \frac{1}{\rho_i} \sum_j m_j (\mathbf{v}_j - \mathbf{v}_i) \cdot \nabla W(\mathbf{r}_{ij}, h), \quad (36)$$

$$\langle \nabla p \rangle_i = \rho_i \sum_j m_j \left( \frac{p_i}{\rho_i^2} + \frac{p_j}{\rho_j^2} \right) \nabla W(\mathbf{r}_{ij}, h), \quad (37)$$

respectively.

To summarize the projection method, first we calculate the predictor velocity  $\mathbf{v}^*$  with a linear solver for Eq. (30), then we solve the PPE (Eq. (32)) implicitly with the same linear solver and, finally, update the next step velocity  $\mathbf{v}^{\beta+1}$  with the corrector step (Eq. (31)). We use fixed wall ghost particles (FWGP) for the enforcement of wall boundary conditions (Adami et al., 2012) in the same way as explained in Morikawa et al. (2019).

#### 4.2. Bingham flow rheology and eddy viscosity

As opposed to Newtonian fluids, the viscosity of non-Newtonian fluids varies according to the adopted rheological model. Here, we

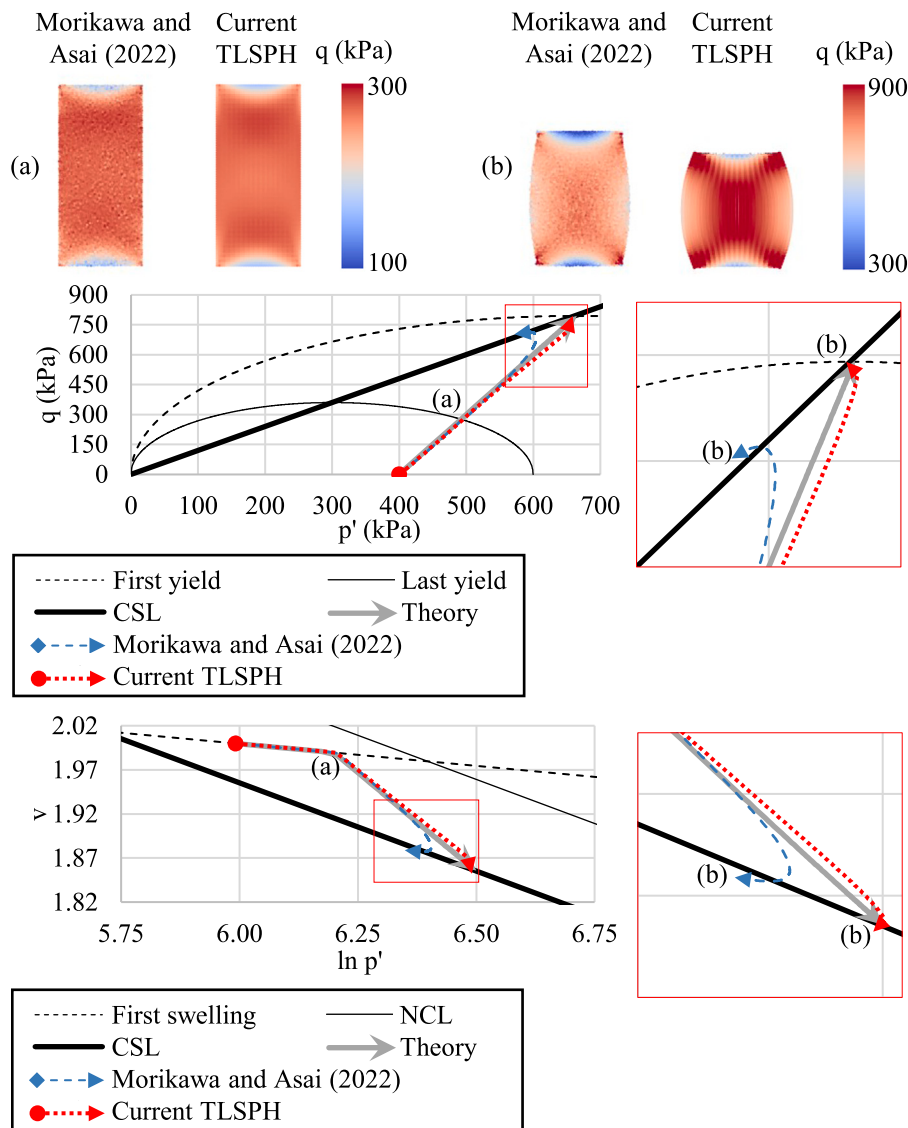


**Fig. 4.** Triaxial compression test: cross section of the specimen right after yielding (a) and in the closest point to the CSL, and the graphs of  $(p', q)$  and  $(\ln p', v)$  spaces for lightly consolidated soil — comparison of proposed method (TLSRH) and previous research (Morikawa and Asai, 2022).

introduce the cross-model to simulate the Bingham plastic fluid, which is expressed as

$$\nu'_f = \nu_{f0} + \frac{\tau_y}{\dot{\gamma}\rho}, \quad (38)$$

where  $\nu_{f0}$  is the initial viscosity,  $\tau_y$  is the yield stress and  $\dot{\gamma}$  is the strain rate calculated as (Violeau and Issa, 2007)

$$\langle \dot{\gamma}^2 \rangle = \frac{1}{2} \sum_j m_j \frac{\rho_i + \rho_j}{\rho_i \rho_j} \frac{\mathbf{r}_{ij} \cdot \nabla W(\mathbf{r}_{ij}, h)}{\mathbf{r}_{ij}^2} |\mathbf{v}_i - \mathbf{v}_j|^2. \quad (39)$$

In this work, we are basically dealing with fluidized soil materials. Hence, we define the yield stress  $\tau_y$  with the Mohr–Coulomb criterion  $\tau_y = c + p \tan \phi'$ , where  $c$  and  $\phi'$  are the cohesion and friction angle, respectively. In addition, to avoid dividing by zero as the fluid velocity decreases (that is,  $\dot{\gamma}$  approaches zero), we define  $\nu_{fMAX}$  as an upper-limit value of the viscosity. Then, we derive the final version for the

Bingham rheology model as

$$\nu'_f = \begin{cases} \nu_{fMAX}, & \text{if } \dot{\gamma} < \frac{c+p \tan \phi'}{\rho(\nu_{fMAX}-\nu_{f0})} \\ \nu_{f0} + \frac{c+p \tan \phi'}{\dot{\gamma}\rho}, & \text{otherwise.} \end{cases} \quad (40)$$

Lastly, we define the fluid viscosity as the summation of the physical viscosity term  $\nu'_f$  and the eddy viscosity term  $\nu_{edd}$ , as proposed by Violeau and Issa (2007). Here,  $\nu_{edd}$  is calculated as

$$\nu_{edd} = (C_s \Delta)^2 \dot{\gamma}, \quad (41)$$

where  $C_s$  is the Smagorinsky constant ( $C_s = 0.2$ ) and  $\Delta = 0.1h$ .

## 5. Coupling mechanism

Solid and fluid phases have different constitutive models to evaluate stress as explained above. The SPH discretization is applied only within same phase particles, but particles on different phases should be coupled through a boundary condition framework. We divide this section into solid to fluid and fluid to solid subsections to facilitate the readers' understanding of these coupling techniques.

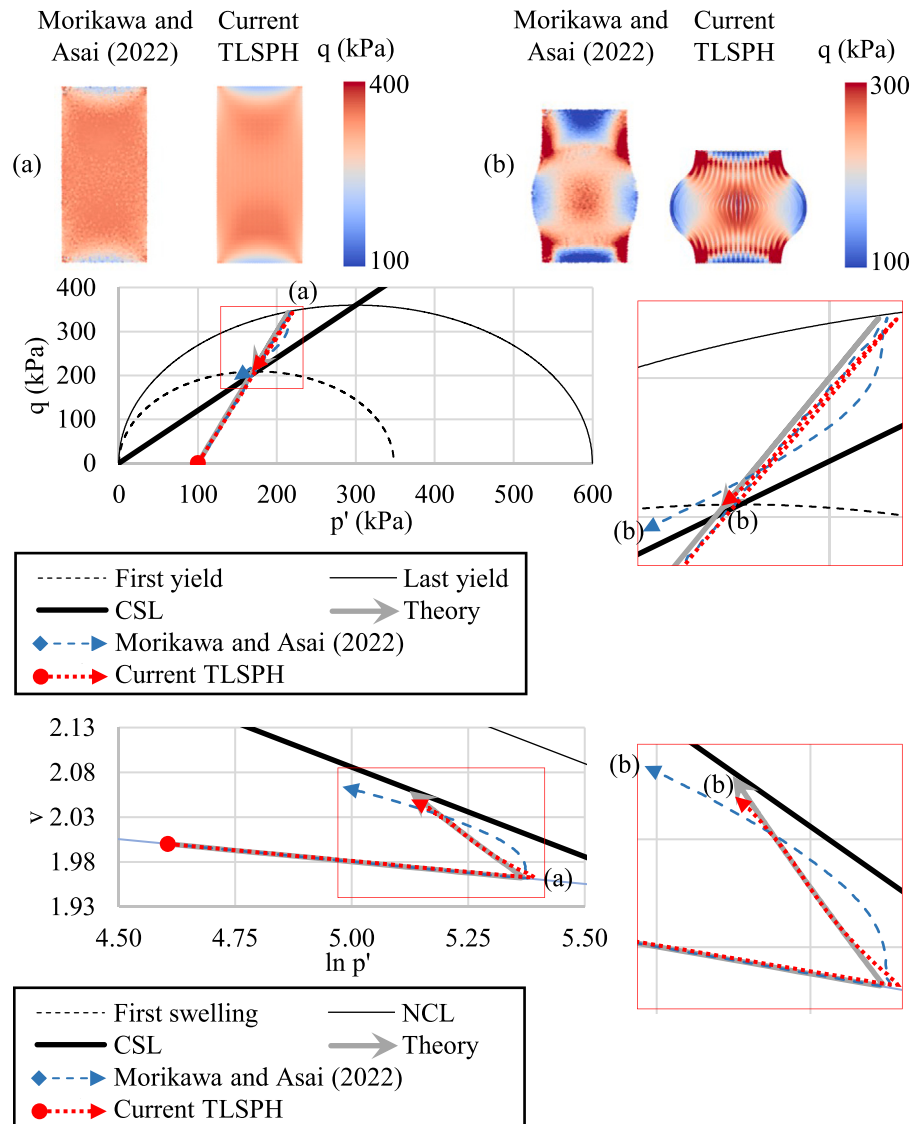


**Fig. 5.** Triaxial compression test: cross section of the specimen right after yielding (a) and in the closest point to the CSL, and the graphs of  $(p', q)$  and  $(\ln p', v)$  spaces for highly consolidated soil — comparison of proposed method (TLSPh) and previous research (Morikawa and Asai, 2022).

### 5.1. Solid to fluid

Let us start this derivation rewriting the Navier-Stokes equation (Eq. (28)) including the coupling force  $\mathbf{f}_{sf}$ , where the subscript  $sf$  signifies “solid to fluid”

$$\frac{D\mathbf{v}}{Dt} = -\frac{1}{\rho}\nabla p + \nu_f \nabla^2 \mathbf{v} + \mathbf{g} + \mathbf{f}_{sf}. \quad (42)$$

The boundary condition for our Fluid Dynamics formulation is based on Fixed Wall Ghost Particles (FWGPs). In this method, the wall particles are treated as an extension of the fluid body with pressure and velocities that adequate the non-penetration and the slip conditions. For the solid to fluid coupling, the idea is similar. Hence, the solid particle is treated as a wall particle where the non-slip condition is applied. Then, we derive the following relation

$$\mathbf{f}_{sf} = \left( -\frac{1}{\rho}\nabla p + \nu_f \nabla^2 \mathbf{v} \right) \Big|_{j \in \text{solid}}. \quad (43)$$

In practice, accounting for the  $\mathbf{f}_{sf}$  term means calculating the gradient of pressure and Laplacian of velocity incorporating both fluid and solid neighboring particles.

### 5.2. Fluid to solid

We start rewriting Eq. (2) to include the “fluid to solid” coupling force  $\mathbf{f}_{fs}$

$$\frac{D\mathbf{v}}{Dt} = \frac{1}{\rho_0} \nabla_0 \cdot \mathbf{P} + \mathbf{g} + \mathbf{f}_{fs}. \quad (44)$$

Contrary to the previous section, the coupling force  $\mathbf{f}_{fs}$  must be explicitly calculated as

$$\mathbf{f}_{sf} = \left( -\frac{1}{\rho}\nabla p + \nu_f \nabla^2 \mathbf{v} \right) \Big|_{j \in \text{fluid}}, \quad (45)$$

which is the reaction equivalent of Eq. (43).

### 5.3. Implementation

A particle  $i$  might be either a solid or a fluid particle. Due to the implicit nature of the fluid part, the coupling force must be calculated concurrently for both phases. With this in mind, the linear momentum

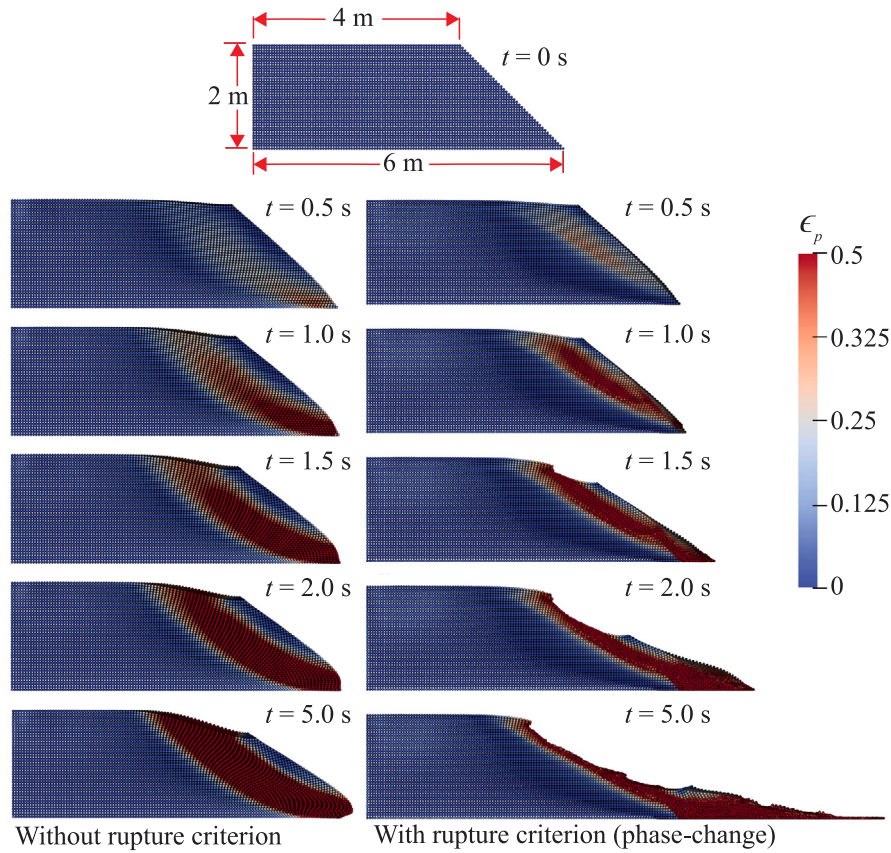


**Fig. 6.** Landslide with phase-change: snapshots of the simulation at different time steps.

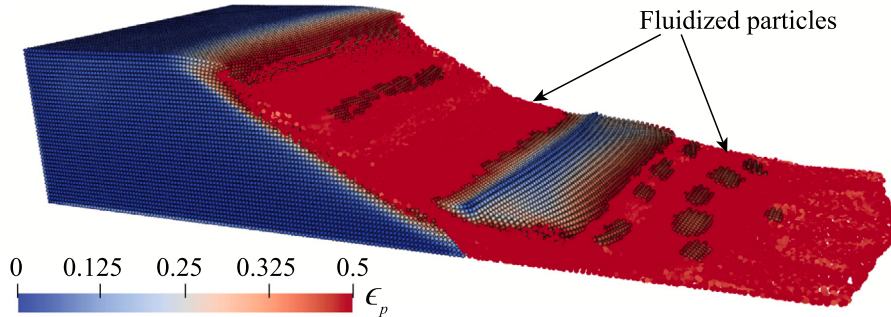


**Fig. 7.** Landslide with phase-change: snapshot of the simulation at  $t = 5$  s highlighting the fluidized particles.

equation for all particles can be written as

$$\frac{D\mathbf{v}}{Dt} = \begin{cases} \left( -\frac{1}{\rho} \nabla p + v_f \nabla^2 \mathbf{v} \right) \Big|_{j \in \text{solid and fluid}} + \mathbf{g}, & \text{if } i \in \text{fluid} \\ \left( \frac{1}{\rho_0} \nabla_0 \cdot \mathbf{P} \right) \Big|_{j \in \text{solid}} + \mathbf{g} + \left( -\frac{1}{\rho} \nabla p + v_f \nabla^2 \mathbf{v} \right) \Big|_{j \in \text{fluid}}, & \text{if } i \in \text{solid}. \end{cases} \quad (46)$$

To maintain the same strategy of the projection method, we divide the above equation into a predictor step

$$\mathbf{v}^* = \mathbf{v}^\beta + \Delta t \begin{cases} \left( v_f \nabla^2 \mathbf{v}^* \right) \Big|_{j \in \text{solid and fluid}} + \mathbf{g}, & \text{if } i \in \text{fluid} \\ \left( \frac{1}{\rho_0} \nabla_0 \cdot \mathbf{P}^\beta \right) \Big|_{j \in \text{solid}} + \mathbf{g} + \left( v_f \nabla^2 \mathbf{v}^* \right) \Big|_{j \in \text{fluid}}, & \text{if } i \in \text{solid}, \end{cases} \quad (47)$$

and a corrector step

$$\mathbf{v}^{\beta+1} = \mathbf{v}^* + \Delta t \begin{cases} \left( -\frac{1}{\rho} \nabla p^{\beta+1} \right) \Big|_{j \in \text{solid and fluid}}, & \text{if } i \in \text{fluid} \\ \left( -\frac{1}{\rho} \nabla p^{\beta+1} \right) \Big|_{j \in \text{fluid}}, & \text{if } i \in \text{solid}. \end{cases} \quad (48)$$

In practice, the solver does not change for target fluid particles, where both solid and fluid neighboring particles are treated equally.

For target solid particles, as expressed in Eq. (47), all matrix coefficients of solid particles referred to as (I) in Fig. 2 (i.e., with no fluid neighbors) are zero, and its source term is the right-hand side of Eq. (7). On the other hand, particles referred to as (II) have the coefficients associated with the fluid particles. Similarly, particles in the (I) zone are not included in the PPE. That is, the PPE is solved only on fluid particles (III) and solid particles with fluid neighbors (II).

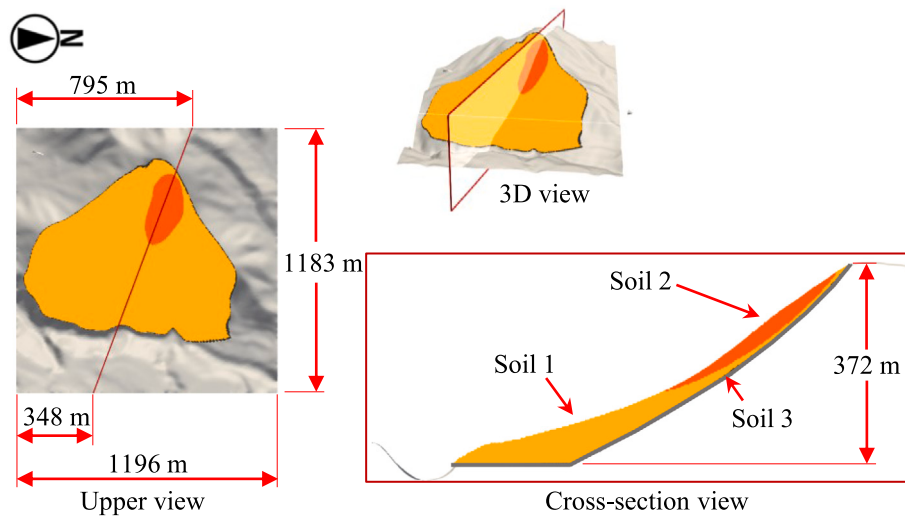


Fig. 8. Aso landslide: modeled soils in both 3D and side views.

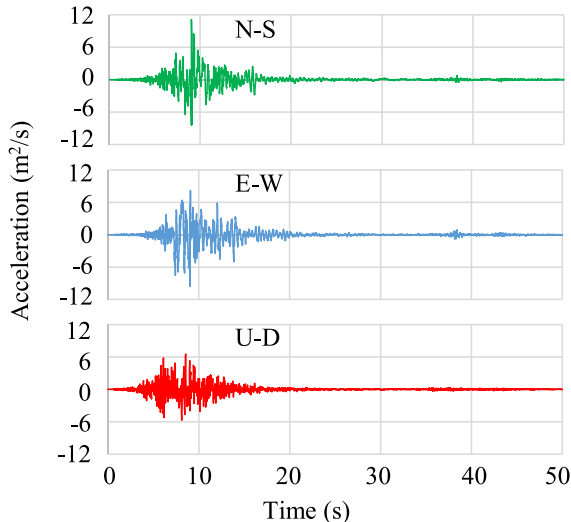


Fig. 9. Aso landslide: earthquake acceleration for North-South (N-S), East-West (E-W) and Up-Down (U-D) directions (JMA, 2021).

As for the maximum time increment  $\Delta t$  allowed for a stable simulation, we utilize the following Courant–Friedrichs–Lewy (CFL) condition (Koshizuka and Oka, 1996; Lee et al., 2016)

$$\Delta t \leq \min \left( C_{\text{CFL}}^f \frac{d}{v_{\max}}, C_{\text{CFL}}^s \frac{d}{c_p} \right), \quad (49)$$

where  $C_{\text{CFL}}^f$  and  $C_{\text{CFL}}^s$  are the CFL coefficients for the fluid and solid parts, respectively. Since the total Lagrangian formulation for the solid part is much more stable than the fluid one, we used  $C_{\text{CFL}}^f = 0.1$  and  $C_{\text{CFL}}^s = 0.5$ .

## 6. Numerical tests

### 6.1. Triaxial compression test

Although the accuracy of the current TLSPH for the hyperelastic solids has already been assessed by Morikawa and Asai (2021), it is still necessary to check whether it is capable of simulating elastoplastic geomaterials. In particular, we intend to demonstrate its robustness in simulating the evolution of the porosity over time (with Eq. (5)).

For that, we simulate the triaxial compression test as a recognized benchmark test in Geomechanics.

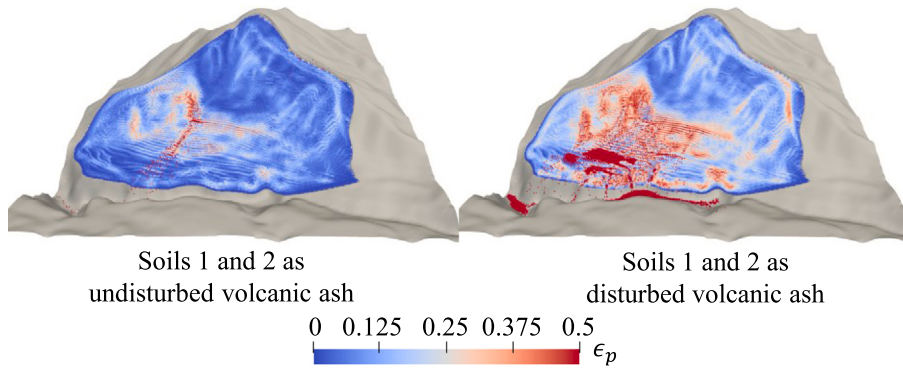
Other researchers such as Pereira et al. (2017) and Zhao et al. (2018) have already reproduced the triaxial compression test with SPH using either Drucker–Prager or Mohr–Coulomb yield criteria. More recently, Morikawa and Asai (2022) have used a soil–water coupling method to simulate this problem in both drained and undrained conditions with the modified Cam–Clay yield criterion. Here, we compare our results with the latter since we use the same yield criterion. Given that we are solving only the soil phase of this problem, our results correspond to the drained condition.

Table 1 summarizes the numerical and material parameters and Fig. 3 illustrates the boundary conditions and geometry. Similarly to Morikawa and Asai (2022), we use ghost particles to define the boundary conditions, where the lateral ghost particles receive the SPH average velocity of the specimen particles located in the interface between specimen and ghost particles.

Figs. 4 and 5 show our results compared with previous research with SPH (Morikawa and Asai, 2022) for lightly and highly consolidated soils, respectively. The results are plotted in graphs of  $q$  over  $p'$  and  $v$  over  $\ln p'$ , here called  $(p', q)$  and  $(\ln p', v)$  spaces. As commonly known in critical state soil mechanics (Schofield and Wroth, 1968), the von Mises stress  $q$  increases together with  $p'$  in a 3:1 ratio during the triaxial compression problem until reaching the critical state line. Then, rupture is defined, and the Modified Cam–Clay model alone is not enough to describe the whole phenomenon anymore.

Finally, we demonstrate the superior accuracy of the current TLSPH compared to the updated Lagrangian technique from Morikawa and Asai (2022), which is more pronounced at the region near the critical state line (CSL). In the previous work (Morikawa and Asai, 2022), the solution rapidly changes its path to the direction of the CSL once it approaches the CSL. This causes the point (b) (closest point to CSL) to happen earlier in their work in comparison to ours. Specifically, point (b) is at  $t = 0.4$  s and  $t = 0.256$  s in Morikawa and Asai (2022) for lightly and highly consolidated, respectively, and  $t = 0.6$  s for both tests in the proposed method.

The lack of accuracy of their method compared to the proposed TLSPH is probably due to the updated Lagrangian nature of their method (Morikawa and Asai, 2022). For example, the more the specimen is compressed, the more particles clump together, which decreases the accuracy of an updated Lagrangian-based SPH method. Also, as the specimen is compressed, the position of lateral particles becomes more disordered, which causes some instabilities. On the other hand, the current TLSPH avoids such problems, since all calculations are conducted in the reference configuration, which has perfect particle distribution.



**Fig. 10.** Aso landslide: snapshots of the simulation with earthquake loading at  $t = 150$  s treating soils 1 and 2 as a single soil mass.

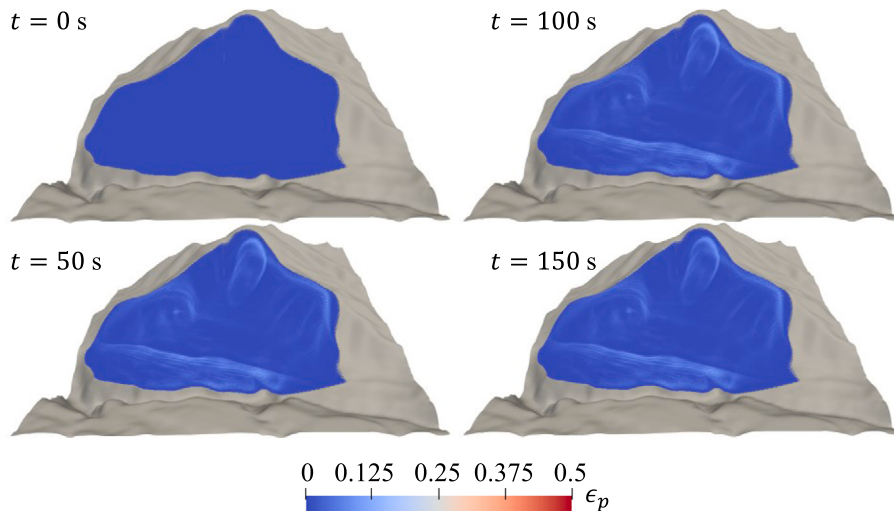


**Fig. 11.** Aso landslide: snapshots at different times without the earthquake loading modeling soil 1 as undisturbed and soil 2 as disturbed volcanic ash.

**Table 1**  
Material and numerical parameters of the triaxial compression test.

Parameter	Symbol	Value
Particle size	$d$	0.002 m
Time increment	$\Delta t$	$10^{-6}$ s
Gradient of swelling line	$\kappa$	0.05
Gradient of the normal consolidation line	$\lambda$	0.2
Poisson's ratio	$\nu$	0.3
Soil density	$\rho_s$	3000 kg/m <sup>3</sup>
Initial porosity	$n_0$	0.5
Initial pre-consolidation pressure	$p_c$	600 kPa
Confining pressure for lightly consolidated soil	$p'_0$	400 kPa
Confining pressure for highly consolidated soil	$p''_0$	100 kPa
Constitutive model of the elastic part		Hencky model
Yield criterion and flow rule		Modified Cam–Clay

## 6.2. Multi-physics landslide

This test is to check the robustness of the proposed method to simulate a generic landslide problem. Table 2 summarizes all parameters used in this numerical simulation, while Fig. 6 shows the geometry of the problem. Here, we compare this problem solved with and without the phase-change algorithm. In other words, we first run this experiment using the TLSPH solely, so the landslide movement is characterized by an elastoplastic material. The second numerical experiment introduces the rupture criterion to particles with accumulated plastic strain higher than 0.5, transforming them into fluidized particles.

Fig. 6 shows the snapshots of the simulations at different time steps. It is visible that transforming the landslide mass into a fluid phase makes this example greatly enhance its realism. To increase clarity, we also show a 3D view of this simulation at  $t = 5$  s highlighting the fluidized particles (Fig. 7). As expected, it is clear that we could simulate a discontinuity between the stable phase and the fluid phase, which is hardly seen in other SPH methods. Also, as expected, some non-fluidized pieces of solid mass at the tip of the slope are carried out by the fluid mass.

## 6.3. Aso landslide

In 2016, an earthquake magnitude M7.3 triggered a series of landslide disasters in Kumamoto prefecture, in Japan. The largest of such landslides occurred at 32.885° N, 130.987° E near the 200 m long Aso bridge (JSECE, 2016), which was destroyed afterward. Dai et al. (2016) have simulated the same landslide with the SPH using a non-Newtonian fluid simulation, where the yield stress is treated as a constant value.

Here, we simulate this problem using the coupled multi-physics proposed method. Hence, as opposed to Dai et al. (2016), we simulate the whole mountain surface to determine both the initiation and the post-failure landslide behavior. As shown in Fig. 8, we modeled three different soils in which soil 1 represents the inner soil layer, soil 2 a weakened soil mass and soil 3 a transition zone between the soil mass and the bedrock layer below.

The parameters chosen were loosely based on JSECE (2016) and Putra (2020), as summarized in Table 3. Specifically, Putra (2020) determined the disturbed and undisturbed shear strength of Aso mountain's

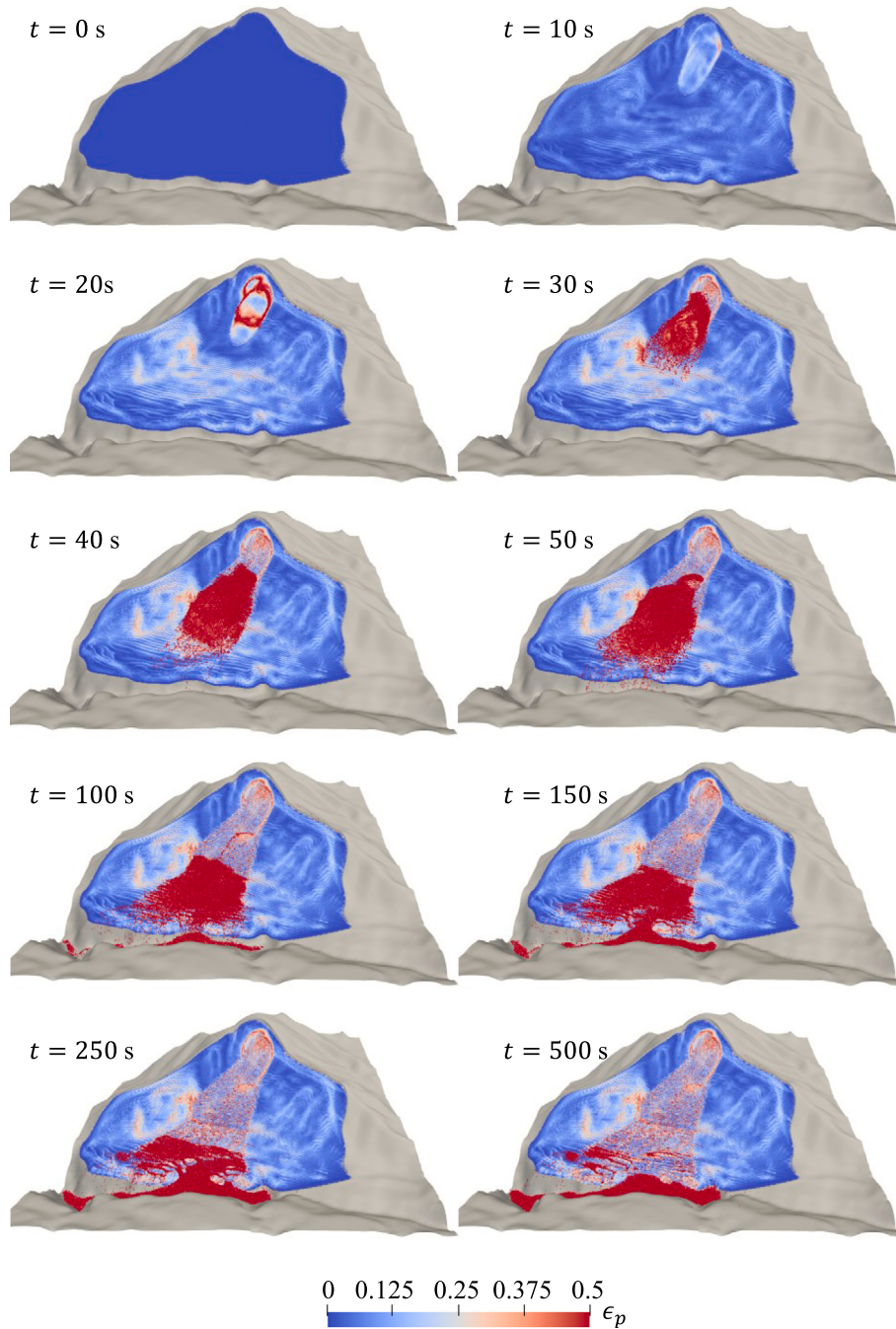


**Fig. 12.** Aso landslide: snapshots at different times with the earthquake loading modeling soil 1 as undisturbed and soil 2 as disturbed volcanic ash — 3D view, colors representing plastic strain.

volcanic ash using shear tests. The earthquake loading is shown in Fig. 9, where the data was retrieved from the Japan Meteorological Agency website (JMA, 2021). This loading is treated as accelerations implemented in the predictor step of both solid and fluid phases (that is, it is included in the vector  $\mathbf{g}$ ).

First, we simulated this problem considering soils 1 and 2 as a single soil mass, while soil 3 as the rock-soil transition. Fig. 10 shows the results using the undisturbed and disturbed volcanic ash parameters. Notice that the landslide does not occur according to the observed data for both simulations. In summary, using only undisturbed volcanic ash parameters, no noticeable landslide occurs, while using the disturbed volcanic ash, a very small landslide occurs at a wrong different location than the one observed in JSECE (2016).

Next, we conducted this simulation modeling soils 1 as undisturbed and soil 2 as disturbed volcanic ash. Fig. 11 shows this simulation for a number of time steps without the earthquake loading. As expected, some plastic deformation occurs to adjust the stress state of the soil, but no landslide occurs.

By applying the earthquake loading, the observed landslide occurred naturally in our numerical simulation, suggesting that the main cause of the landslide might be the existence of weakened soil in the region modeled as soil 2. Figs. 12 and 13 show a 3D view of a step-by-step illustration of the landslide initiation and post-failure behavior.

In addition, we plotted Figs. 14 and 15 to show a side view of this landslide at different time-steps. Notice that the proposed method can simulate two different erosion patterns: a thin layer of eroded path on

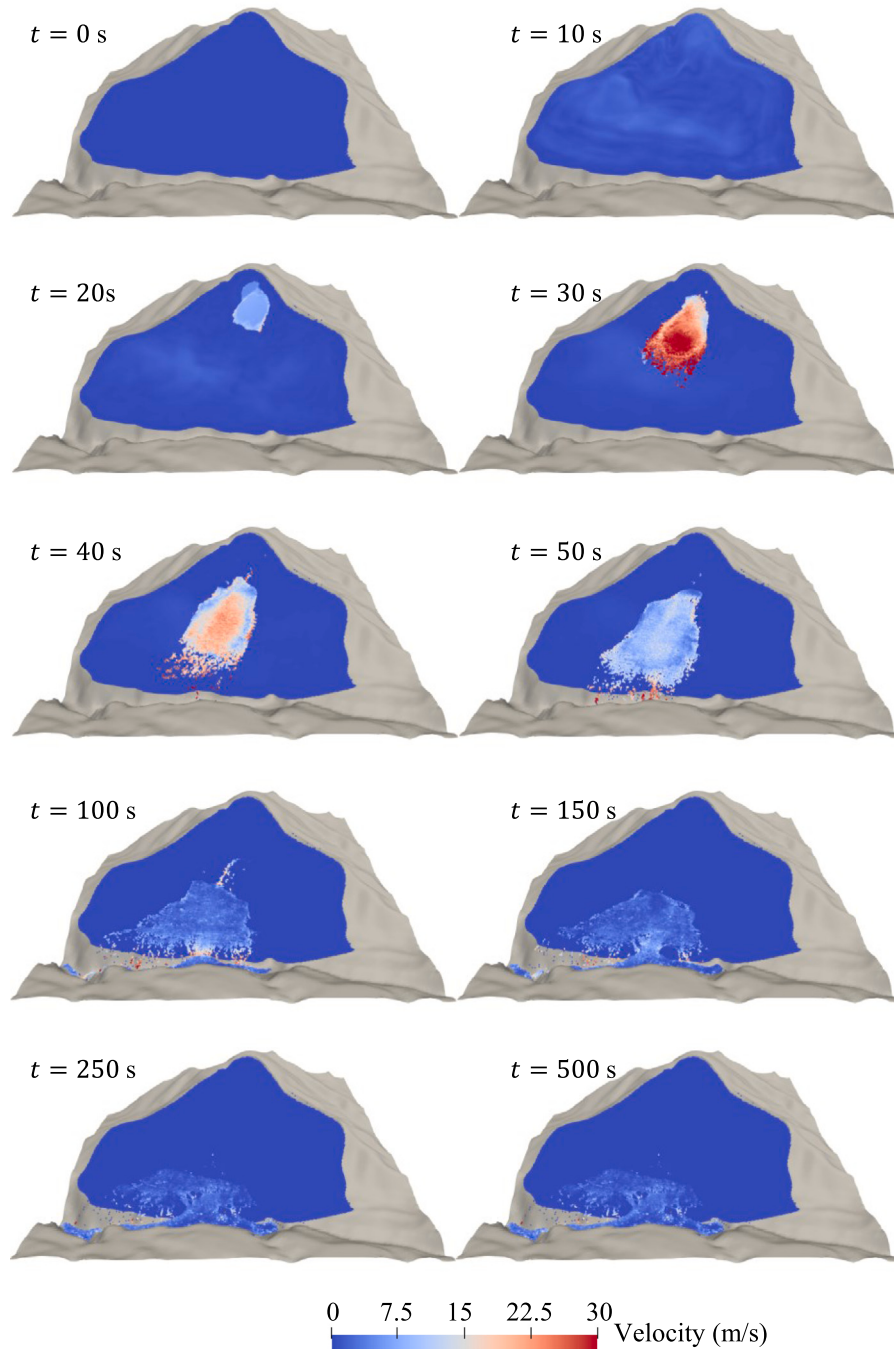


**Fig. 13.** Aso landslide: snapshots at different times with the earthquake loading modeling soil 1 as undisturbed and soil 2 as disturbed volcanic ash — 3D view, colors representing velocity.

the intermediate mountain surface (here called “thin erosion”) and a thicker layer of eroded material at the base of the mountain (here called “thick erosion”), as illustrated in Fig. 16b.

Following, let us show a qualitative comparison of the above-mentioned trends between our simulated results and the observed data. Fig. 16a reproduces the topographical data of the slope before and after the landslide occurrence. Erosion occurred in regions where the observed topographical data before the landslide is above the one after the

landslide; on the contrary, it was observed deposited material (JSECE, 2016). Also, it is clear that the erosion pattern of the base of the mountain differs considerably from the intermediate surface. In JSECE (2016), they call the thicker layer of eroded material at the base of the mountain as “secondary landslide”.

Comparing Figs. 16a and 16b, we may conclude that the observed erosion on the intermediate mountain surface has occurred at a thinner layer of soil in comparison with our results (thin erosion). This may be

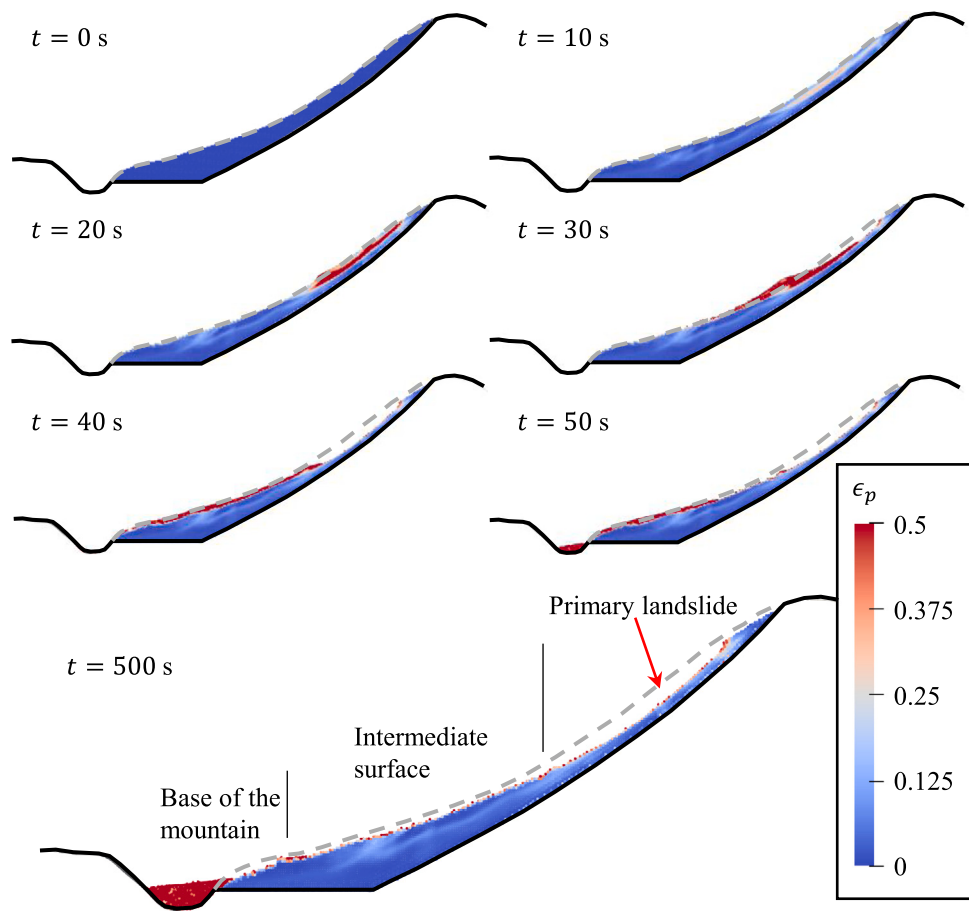


**Fig. 14.** Aso landslide: snapshots at different times with the earthquake loading modeling soil 1 as undisturbed and soil 2 as disturbed volcanic ash — side view, colors representing plastic strain.

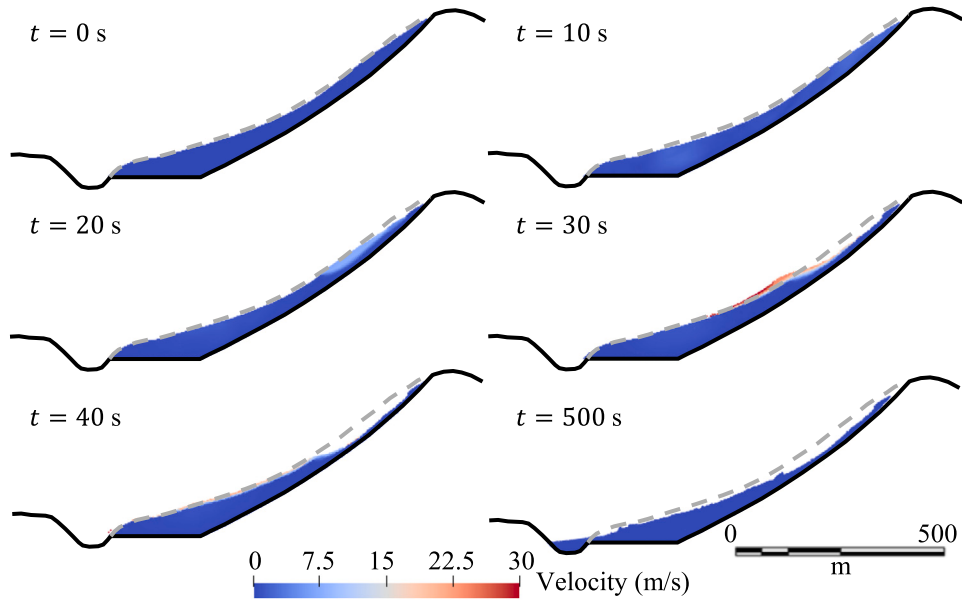


**Fig. 15.** Aso landslide: snapshots at different times with the earthquake loading modeling soil 1 as undisturbed and soil 2 as disturbed volcanic ash — side view, colors representing velocity.

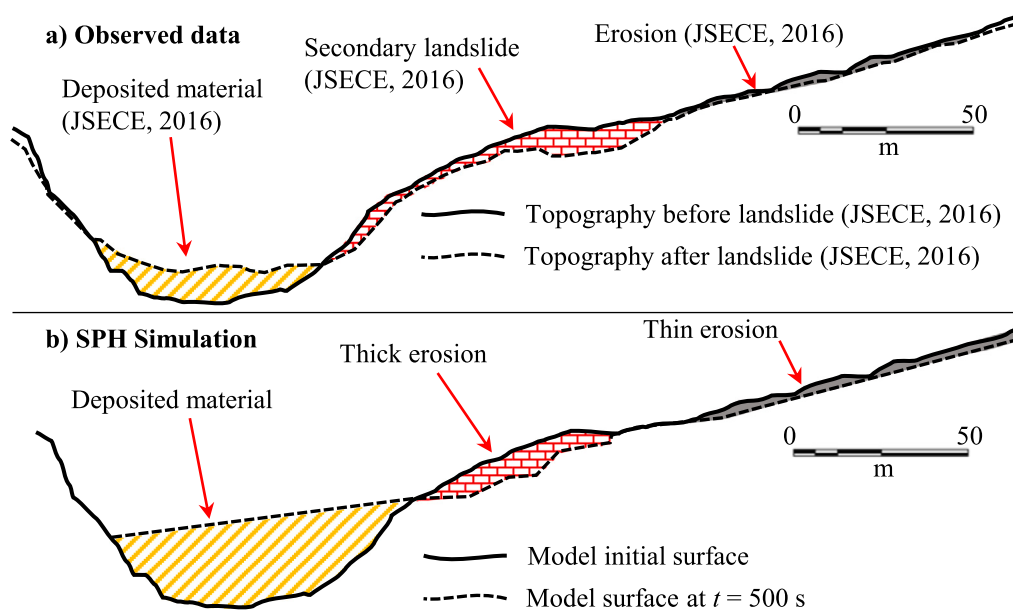


Fig. 16. Aso landslide: cross section view comparing (a) observed data (JSECE, 2016) and (b) SPH simulation at  $t = 500$  s.

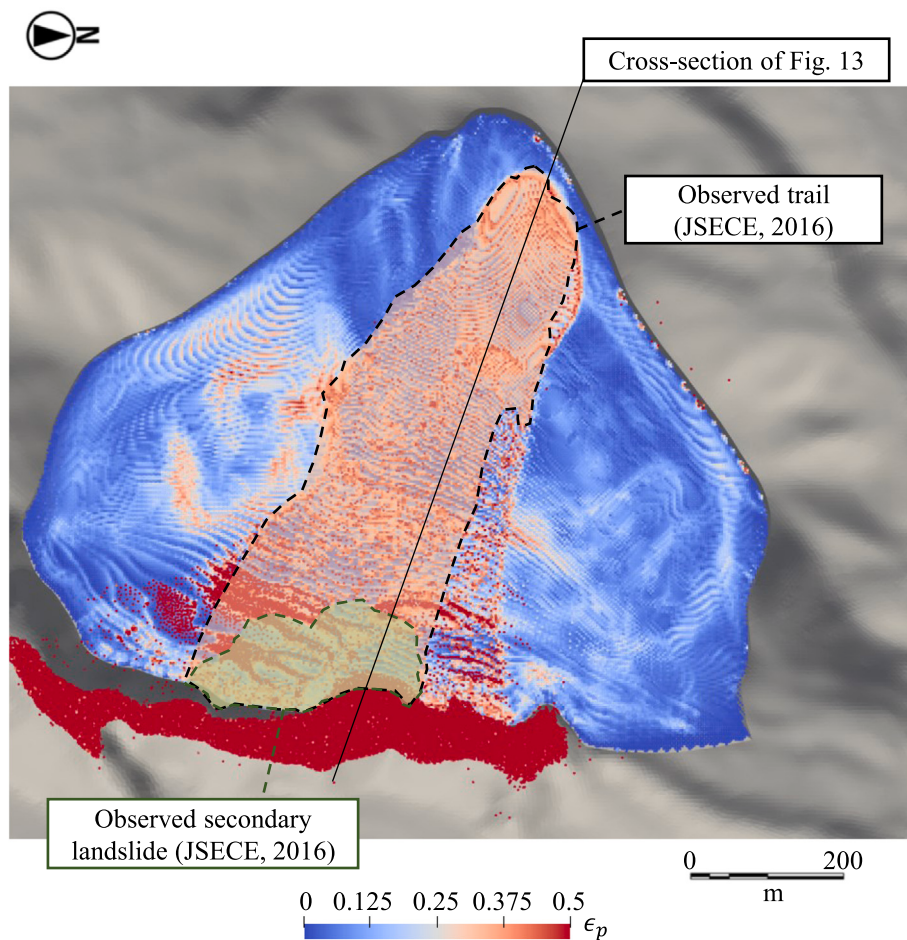


Fig. 17. Aso landslide: upper view of the simulation modeling soil 1 as undisturbed and soil 2 as disturbed volcanic ash at  $t = 500$  s in comparison with observed landslide trail and secondary landslide according to JSECE (2016).

**Table 2**  
Material and numerical parameters of the slope failure test with phase-change.

Parameter	Symbol	Value
General parameters		
Particle size	$d$	0.05 m
Time increment	$\Delta t$	$10^{-4}$ s
Solid parameters		
Young's modulus	$E$	0.84 MPa
Poisson's ratio	$\nu$	0.45
Soil density	$\rho_s$	1655 kg/m <sup>3</sup>
Friction angle	$\phi'$	19.5°
Initial cohesion	$c_0$	1 kPa
Dilatancy angle	$\psi$	0°
Hardening coefficient	$H$	-0.1 kPa
Constitutive model of the elastic part		Hencky model
Yield criterion and flow rule		Drucker-Prager
Fluid parameters		
Fluid phase initial viscosity	$\nu_{f0}$	$10^{-3}$ m <sup>2</sup> /s
Fluid phase maximum viscosity	$\nu_{fMAX}$	$10^4$ m <sup>2</sup> /s
Friction angle	$\phi'$	19.5°
Cohesion	$c$	0.01 kPa

**Table 3**  
Material and numerical parameters of the Aso landslide as a multi-physics problem.

Parameter	Symbol	Value
General parameters		
Particle size	$d$	3 m
Time increment	$\Delta t$	$10^{-3}$ s
Young's modulus	$E$	50 MPa
Poisson's ratio	$\nu$	0.3
Soil density	$\rho_s$	1143.88 kg/m <sup>3</sup>
Constitutive model of the elastic part		Hencky model
Yield criterion and flow rule		Drucker-Prager
Undisturbed volcanic ash		
Friction angle	$\phi'$	35.5°
Initial cohesion	$c_0$	24.6 kPa
Dilatancy angle	$\psi$	0°
Hardening coefficient	$H$	-5 kPa
Disturbed volcanic ash		
Friction angle	$\phi'$	35°
Initial cohesion	$c_0$	11.75 kPa
Dilatancy angle	$\psi$	0°
Hardening coefficient	$H$	-5 kPa
Rock-soil transition		
Friction angle	$\phi'$	35.5°
Initial cohesion	$c_0$	60 kPa
Dilatancy angle	$\psi$	0°
Hardening coefficient	$H$	0 kPa
Fluid parameters		
Fluid phase initial viscosity	$\nu_{f0}$	$10^{-3}$ m <sup>2</sup> /s
Fluid phase maximum viscosity	$\nu_{fMAX}$	$10^4$ m <sup>2</sup> /s
Friction angle	$\phi'$	20°
Cohesion	$c$	0.1 kPa

explained by the large particle diameter of 3 m used in the simulation and by numerical errors. For the base of the mountain, we observe that the thick erosion in our simulation occurred in a region near the observed secondary landslide, although the shapes differ considerably. As for the deposited material, it is not a fair comparison since the topographical data has been taken many days after the event, while the simulated result lasts only 500 s.

For completeness, we plotted an upper view of the simulation at  $t = 500$  (Fig. 17) over the observed data from JSECE (2016) to compare with the observed landslide trail. Although not a perfect fit,

we conclude that the pathway in which the soil eroded in our numerical simulation coincides reasonably with the observed landslide trail.

In quantitative terms, JSECE (2016) reported an estimate of 540.000 m<sup>3</sup> of generated sediment. In comparison, our simulation resulted in a total of 33.390 fluidized particles at  $t = 500$  s, which, considering that each particle has 27 m<sup>3</sup> of volume, a total of 901.530 m<sup>3</sup> of generated sediment. This difference can be explained by a few factors. First, we may have defined a larger volume of weakened soil (soil 2) if compared to the real situation. Second, for practical reasons, we have chosen a large particle diameter ( $d = 3$  m). As a result, it is impossible to represent a thinner layer of eroded material at the slope surface (Fig. 16). Third, not every particle that became fluidized in our simulation necessarily produces sediment, as can be seen in Fig. 17. In conclusion, it is expected that our simulation produces more fluidized particles than the observed phenomena. As for the landslide dynamics, our simulation resulted in an average maximum velocity of 35 m/s at  $t = 30$  s. However, we could not obtain any observational data on this matter.

Lastly, we must acknowledge a few shortcomings of this simulation. Mainly, the weakened zone (soil 2) has been chosen in order to roughly agree with the observed primary landslide, which is usually not known a priori. Also, other material parameters such as the material apparent viscosity after detachment as also unknown, since no experiments were conducted to quantitatively estimate it. However, we believe that it was a fair attempt on simulating this phenomenon and that it is a proof of the potential of the proposed method.

## 7. Conclusions

In this work, we propose a phase-change approach to simulate landslide at high deformation levels. The stable soil is simulated with Solid Mechanics equations using the TLSPH method, while the landslide propagation with Fluid Dynamics using the IISPH method. For the TLSPH, we introduced a finite strain elastoplastic constitutive model with the logarithmic strain, in which the Hencky model and the elastic-predictor/plastic-corrector return mapping are applied. Then, particles that surpass a specific plastic deformation threshold are designated to change their phase to a fluid state. Finally, we present the coupling technique as a conventional FSI problem.

With the numerical simulation of the triaxial compression problem at the drained condition, we demonstrate that the proposed TLSPH is capable of simulating Geomechanics problems with higher accuracy than previous study based on the updated Lagrangian framework (Morikawa and Asai, 2022). Specifically, the total Lagrangian nature of the proposed method solves the problem of particle clumping and instabilities on the lateral particles of the specimen. As a result, our solution becomes highly accurate from beginning to end, as opposed to Morikawa and Asai (2022)'s work which loses accuracy near the CSL. Next, we present a conceptual example of a simple landslide simulation, where the phase-change approach significantly increases its realism.

Finally, we show an application of the proposed method in a realistic scenario with the simulation of the Aso landslide. It may be the first attempt to simulate this problem from the detachment of the landslide mass to its post-failure behavior. No landslide was detected in the simulation without the earthquake loading, while the landslides were a natural consequence of the observed earthquake. We achieved good agreements with observational data (JSECE, 2016) referring to the material parameters of two different samples for undisturbed volcanic ash and disturbed volcanic ash tested by Putra (2020). Furthermore, we realized from our simulations that one of the leading causes of the landslide may be the presence of a weakened soil mass within the mountain surface labeled as "soil 2".

However, we acknowledge that the simulation had a few arbitrary settings that facilitated the agreement with the observational data. Namely, we defined soil 2 as to roughly agree with the topography of

the primary landslide, and we chose some material parameters such as the fluidized soil viscosity without any prior experimental data.

The main objective of this simulation is to demonstrate the potential of the method, rather than being an ultimate simulation of Aso landslide. With that in mind, we conclude that the simulation was successful for our purposes. For future works, we intent to use the proposed method including more reliable assessments on the material properties in terms of both rheology and spatial distribution.

#### CRediT authorship contribution statement

**Daniel S. Morikawa:** Conceptualization, Methodology, Software, Formal analysis, Investigation, Resources, Data curation, Writing – original draft, Writing – review & editing, Visualization, Project administration, Funding acquisition. **Mitsuteru Asai:** Methodology, Software, Formal analysis, Resources, Data curation, Writing – review & editing, Supervision, Project administration, Funding acquisition.

#### Declaration of competing interest

The authors declare that they have no known competing financial interests or personal relationships that could have appeared to influence the work reported in this paper.

#### Acknowledgments

The first author is supported by the Japan Society for the Promotion of Science (JSPS) through the Research Fellowship for Young Scientists.

This work was supported by the Japan Society for the Promotion of Science (JSPS) KAKENHI Grant Number 20J13114, JP-20H02418, 19H01098, and 19H00812. In addition, this study was supported by the Earthquake Research Institute (ERI) from the University of Tokyo, JURP 2021-S-B201. We also received computational environment support through the Joint Usage/Research Center for Interdisciplinary Large-scale Information Infrastructures (JHPCN) in Japan (Project ID: jh200034-NAH and jh200015-NAH).

#### Appendix A. Return mapping with Drucker–Prager yield criterion

Here we briefly introduce a return mapping algorithm using the non-associative Drucker–Prager yield criterion with linear hardening. All relationships are written as a function of the mean effective stress  $p'$ , the deviatoric stress  $s$  and the second invariant of the deviatoric stress  $J_2$ .

The model parameters are  $c$ , the soil cohesion,  $\xi$  and  $\eta$ , parameters related to friction angle  $\phi'$ , and  $\bar{\eta}$ , a parameter related to the dilatancy angle  $\psi$ . In this study we use  $\xi$ ,  $\eta$  and  $\bar{\eta}$  that circumscribes the Mohr's circle:

$$\xi = \frac{6cc\cos\phi'}{\sqrt{3}(3-\sin\phi')}; \quad \eta = \frac{2\sin\phi'}{\sqrt{3}(3-\sin\phi')}; \quad \bar{\eta} = \frac{2\sin\psi}{\sqrt{3}(3-\sin\psi)}. \quad (\text{A.1})$$

Algorithm 1 shows in an easy-to-follow way the return mapping for the Drucker–Prager model. For a detailed explanation of the algorithm, please refer to [de Souza Neto et al. \(2008\)](#), for example.

#### Appendix B. Return mapping with modified Cam–Clay yield criterion

The modified Cam–Clay model (MCC) is a yield criterion based on critical state Soil Mechanics. As opposed to other classical models such as Mohr–Coulomb or Drucker–Prager, the MCC set equations not only for the stress–strain relationship, but also for the overall density of the material, here represented by the specific volume  $v = 1 + e = 1 + n/(1 - n)$ .

The two main variables related to the stress response of the material are the mean effective stress  $p'$  and the von Mises stress  $q$ .  $\lambda$  and  $\kappa$  are

#### Algorithm 1 Drucker–Prager

---

**Input:**  $\sigma^{\text{trial}}$ ,  $\epsilon_p^\beta$   
**Output:**  $\sigma^{\beta+1}$ ,  $\epsilon_p^{\beta+1}$

Trial state:  $\epsilon_p^{\text{trial}} = \epsilon_p^\beta$  and  $c^{\text{trial}} = c_0 + H\epsilon_p^{\text{trial}} \geq c_r$   
Calculate:  
 $p'^{\text{trial}} = \frac{\sigma_{xx}^{\text{trial}} + \sigma_{yy}^{\text{trial}} + \sigma_{zz}^{\text{trial}}}{3}$   
 $\mathbf{s}^{\text{trial}} = \sigma^{\text{trial}} - p'^{\text{trial}}\mathbf{I}$   
 $J_2^{\text{trial}} = \frac{1}{2}\mathbf{s}^{\text{trial}} : \mathbf{s}^{\text{trial}}$   
**if**  $\varphi^{\text{trial}} \leq 0$  **then**  
    Elastic deformation:  $\sigma^{\beta+1} = \sigma^{\text{trial}}$   
**else**  
    Plastic deformation:  
    (a)  $\sigma^{\beta+1}$  is on the smooth portion of  $\varphi$   
 $\Delta\gamma = \frac{\varphi^{\text{trial}}}{\mu + \bar{\eta}K} + \xi^2 H$   
 $\sigma^{(a)} = \left(1 - \frac{\mu\Delta\gamma}{\sqrt{J_2^{\text{trial}}}}\right)\mathbf{s}^{\text{trial}} + (p'^{\text{trial}} - K\bar{\eta}\Delta\gamma)\mathbf{I}$   
 $\epsilon_p^{\text{trial}} = \epsilon_p^\beta + \xi\Delta\gamma$   
    Check (a): if  $\sqrt{J_2^{\text{trial}}} - \mu\Delta\gamma \geq 0$  **then**  
         $\sigma^{\beta+1} = \sigma^{(a)}$ ,  $\epsilon_p^{\beta+1} = \epsilon_p^{\text{trial}}$  and go to (c)  
    (b)  $\sigma^{\beta+1}$  is on the apex of  $\varphi$   
 $\Delta\gamma = \frac{p'^{\text{trial}} - (\xi/\eta)c}{(\xi^2/\eta^2)H + K}$   
 $\epsilon_p^{\text{trial}} = \epsilon_p^\beta + (\xi/\eta)\Delta\gamma$   
 $\sigma^{(b)} = (p'^{\text{trial}} - K\Delta\gamma)\mathbf{I}$   
 $\sigma^{\beta+1} = \sigma^{(a)}$ ,  $\epsilon_p^{\beta+1} = \epsilon_p^{\text{trial}}$   
    (c) End of return map  
**end if**

---

the gradient of the normal consolidation line (NCL) and the swelling line, respectively. For the Newton–Raphson routine, we need to define the following equations:

$$R_1^k = (p'^k)^2 + p_c^k p'^k + (q^k/M)^2, \quad (\text{B.1})$$

$$R_2^k = (\Delta\epsilon_v^p)^k + (\Delta\gamma)^k (2p'^k + p_c^k), \quad (\text{B.2})$$

$$\mathbf{J}^k = \begin{bmatrix} \frac{\partial R_1}{\partial \Delta\gamma} & \frac{\partial R_1}{\partial \Delta\epsilon_v^p} \\ \frac{\partial R_2}{\partial \Delta\gamma} & \frac{\partial R_2}{\partial \Delta\epsilon_v^p} \end{bmatrix}^k, \quad (\text{B.3})$$

$$\frac{\partial R_1}{\partial \Delta\gamma} = -\frac{12\mu}{M^2 + 6\mu\Delta\gamma} \left(\frac{q}{M}\right)^2, \quad (\text{B.4})$$

$$\frac{\partial R_1}{\partial \Delta\epsilon_v^p} = 2p'K + p_cK + \frac{v}{\lambda - \kappa}p'p_c, \quad (\text{B.5})$$

$$\frac{\partial R_2}{\partial \Delta\gamma} = 2p' + p_c, \quad (\text{B.6})$$

$$\frac{\partial R_2}{\partial \Delta\epsilon_v^p} = 1 + \Delta\gamma \left(2K + \frac{v}{\lambda - \kappa}p_c\right), \quad (\text{B.7})$$

where  $k$  represents a step in the Newton–Raphson. Algorithm 2 presents a straight forward methodology to conduct the return mapping using the modified Cam–Clay. Again, readers interested in understanding the details of this algorithm should refer to [de Souza Neto et al. \(2008\)](#), [Zienkiewicz et al. \(1999\)](#) or other classical authors in this subject.

**Algorithm 2** Modified Cam–Clay return map

---

**Input:**  $\sigma^{\text{trial}}, p_c^\beta$   
**Output:**  $\sigma^{\beta+1}, p_c^{\beta+1}$

**Calculate:**

$$p'^{\text{trial}} = \frac{\sigma_{xx}^{\text{trial}} + \sigma_{yy}^{\text{trial}} + \sigma_{zz}^{\text{trial}}}{3}$$

$$\mathbf{s}^{\text{trial}} = \sigma^{\text{trial}} - p'^{\text{trial}} \mathbf{I} \text{ and } q^{\text{trial}} = \sqrt{\frac{3}{2} \mathbf{s}^{\text{trial}} : \mathbf{s}^{\text{trial}}}$$

$$K = vp'/\kappa \text{ and } \mu = 3K(1-2\nu)/(2(1+\nu))$$

$$\varphi^{\text{trial}} = (p'^{\text{trial}})^2 + p_c^\beta p'^{\text{trial}} + (q^{\text{trial}}/M)^2$$

**if**  $\varphi^{\text{trial}} \leq 0$  **then**

Elastic deformation:  $\sigma^{\beta+1} = \sigma^{\text{trial}}$

**else**

Plastic deformation:

(a) Preparing for the Newton–Raphson:

Set:  $p_c^0 = p_c^\beta$ ,  $p'^0 = p'^{\text{trial}}$  and  $q^0 = q^{\text{trial}}$

Set:  $k = 0$ ,  $\Delta\gamma = 0$  and  $\Delta\epsilon_v^p = 0$

(b) Newton–Raphson:

**do while** ( $\text{error} > \delta$ )

Calculate  $R_1^k, R_2^k$  with Eqs. (B.1) and (B.2)

Calculate the Jacobian  $\mathbf{J}^k$  with Eq. (B.3)

Solve  $\begin{pmatrix} \Delta\gamma \\ \Delta\epsilon_v^p \end{pmatrix}^{k+1} = \begin{pmatrix} \Delta\gamma \\ \Delta\epsilon_v^p \end{pmatrix}^k - (\mathbf{J}^k)^{-1} \begin{pmatrix} R_1 \\ R_2 \end{pmatrix}^k$

Update:

$p^{k+1} = p^{\text{trial}} + K\Delta\epsilon_v^p$

$q^{k+1} = \left( \frac{M^2}{M^2 + 6\mu\Delta\gamma} \right) q^{\text{trial}}$

$p_c^{k+1} = \frac{p_c^{\text{trial}}}{1 - \Delta\epsilon_v^p(\lambda - \kappa)}$

$K = vp'/\kappa \text{ and } \mu = 3K(1-2\nu)/(2(1+\nu))$

Error:  $\text{error} = \sqrt{(R_1^{k+1})^2 + (R_2^{k+1})^2}$

$k = k + 1$

**end do**

(c) Retrieve:

$p'^{\beta+1} = p^{\text{trial}} + K\Delta\epsilon_v^p$

$\mathbf{s}^{\beta+1} = \left( \frac{M^2}{M^2 + 6\mu\Delta\gamma} \right) \mathbf{s}^{\text{trial}}$

$\sigma^{\beta+1} = \mathbf{s}^{\beta+1} + p'^{\beta+1} \mathbf{I}$

$p_c^{\beta+1} = \frac{p_c^{\text{trial}}}{1 - \Delta\epsilon_v^p(\lambda - \kappa)}$

(d) End of return map

**end if**

---

**References**

- Adami, S., Hu, X., Adams, N., 2012. A generalized wall boundary condition for smoothed particle hydrodynamics. *J. Comput. Phys.* 231, 7057–7075. <http://dx.doi.org/10.1016/j.jcp.2012.05.005>.
- An, H., Ouyang, C., Wang, F., Xu, Q., Wang, D., Yang, W., Fan, T., 2022. Comprehensive analysis and numerical simulation of a large debris flow in the meilong catchment, China. *Eng. Geol.* 298, 106546. <http://dx.doi.org/10.1016/j.enggeo.2022.106546>, URL: <https://www.sciencedirect.com/science/article/pii/S001379522200031X>.
- Antoci, C., Gallati, M., Sibilla, S., 2007. Numerical simulation of fluid-structure interaction by SPH. *Comput. Struct.* 85, 879–890. <http://dx.doi.org/10.1016/j.compstruc.2007.01.002>.
- Asai, M., Aly, A., Sonoda, Y., Sakai, Y., 2012. A stabilized incompressible SPH method by relaxing the density invariance condition. *J. Appl. Math.* 2012, 24. <http://dx.doi.org/10.1155/2012/139583>.
- Bandara, S., Soga, K., 2015. Coupling of soil deformation and pore fluid flow using material point method. *Comput. Geotech.* 63, 199–214. <http://dx.doi.org/10.1016/j.comgeo.2014.09.009>.
- Belytschko, T., Guo, Y., Liu, W.K., Xiao, S.P., 2000a. A unified stability analysis of meshless particle methods. *Int. J. Meth. Engrg.* 48, 1359–1400. [http://dx.doi.org/10.1002/1097-0207\(20000730\)48:9<1359::AID-NME829>3.0.CO;2-U](http://dx.doi.org/10.1002/1097-0207(20000730)48:9<1359::AID-NME829>3.0.CO;2-U).
- Belytschko, T., Liu, W., Moran, B., 2000b. Nonlinear Finite Elements for Continua and Structures. John Wiley & Sons, Ltd.
- Beuth, L., Benz, T., Vermeer, P., Wickowski, Z., 2008. Large deformation analysis using a quasi-static material point method. *J. Theoret. Appl. Mech.* 38, 45–60.
- Beuth, L., Wieckowski, Z., Vermeer, P., 2010. Solution of quasi-static large-strain problems by the material point method. *Int. J. Numer. Anal. Methods Geomech.* 35, 1451–1465. <http://dx.doi.org/10.1002/nag.965>.
- Biot, M., 1956. Theory of propagation of elastic waves in a fluid-saturated porous solid. I. Low-frequency range. *J. Acoust. Soc. Am.* 28–2, 168–178. <http://dx.doi.org/10.1121/1.1908239>.
- Bishop, A., 1955. The use of the slip circle in the stability analysis of slopes. *Geotechnique* 5, 7–17. <http://dx.doi.org/10.1680/geot.1955.5.1.7>.
- Blanc, T., Pastor, M., 2012. A stabilized fractional step, Runge–Kutta Taylor SPH algorithm for coupled problems in geomechanics. *Comput. Methods Appl. Mech. Engrg.* 221–222, 41–53. <http://dx.doi.org/10.1016/j.cma.2012.02.006>.
- Bonet, J., Lok, T.-S., 1999. Variational and momentum preservation aspects of smoothed particle hydrodynamics formulations. *Comput. Methods Appl. Mech. Engrg.* 180, 97–115. [http://dx.doi.org/10.1016/S0045-7825\(99\)00051-1](http://dx.doi.org/10.1016/S0045-7825(99)00051-1).
- Bui, H., Fukagawa, R., 2009. A first attempt to solve soil-water coupled problem by SPH. *Jpn. Terramechanics* 29, 33–38.
- Bui, H., Nguyen, G., 2017. A coupled fluid-solid SPH approach to modelling flow through deformable porous media. *Int. J. Solids Struct.* 125, 244–264. <http://dx.doi.org/10.1016/j.ijsolstr.2017.06.022>.
- Cascini, L., Cuomo, S., Pastor, M., Sacco, C., 2013. Modelling the post-failure stage of rainfall-induced landslides of the flow type. *Can. Geotech. J.* 50 (9), 924–934. <http://dx.doi.org/10.1139/cjg-2012-0375>.
- Cascini, L., Cuomo, S., Pastor, M., Sorbino, G., Piciullo, L., 2014. SPH run-out modelling of channelised landslides of the flow type. *Geomorphology* 214, 502–513. <http://dx.doi.org/10.1016/j.geomorph.2014.02.031>.
- Cascini, L., Cuomo, S., Pastor, M., Sorbino, G., 2010. Modeling of rainfall-induced shallow landslides of the flow-type. *J. Geotech. Geoenviron. Eng.* 136, [http://dx.doi.org/10.1061/\(ASCE\)GT.1943-5606.0000182](http://dx.doi.org/10.1061/(ASCE)GT.1943-5606.0000182).
- Culmann, C., 1875. Die Graphische Statik. Meyer and Zeller, Zurich.
- Dai, Z., Wang, F., Huang, Y., Song, K., Iio, A., 2016. SPH-based numerical modeling for the post-failure behavior of the landslides triggered by the 2016 Kumamoto earthquake. *Geoenviron. Disasters* 3, 24. <http://dx.doi.org/10.1186/s40677-016-0058-5>.
- de Souza Neto, E., Perić, D., Owen, D., 2008. Computational Methods for Plasticity: Theory and Applications. John Wiley & Sons, Ltd, <http://dx.doi.org/10.1002/9780470694626>.
- Ganzenmüller, G., 2015. An hourglass control algorithm for Lagrangian smooth particle hydrodynamics. *Comput. Methods Appl. Mech. Engrg.* 286, 87–106. <http://dx.doi.org/10.1016/j.cma.2014.12.005>.
- Gingold, R., Monaghan, J., 1977. Smoothed particle hydrodynamics: theory and application to non-spherical stars. *Astron. Soc.* 181, 375–389. <http://dx.doi.org/10.1093/mnras/181.3.375>.
- Gray, J., Monaghan, J., Swift, R., 2001. SPH elastic dynamics. *Comput. Methods Appl. Mech. Engrg.* 190, 6641–6662. [http://dx.doi.org/10.1016/S0045-7825\(01\)00254-7](http://dx.doi.org/10.1016/S0045-7825(01)00254-7).
- Han, Z., Su, B., Li, Y., Wang, W., Wang, W., Huang, J., Chen, G., 2019. Numerical simulation of debris-flow behavior based on the SPH method incorporating the Herschel–Bulkley–Papanastasiou rheology model. *Eng. Geol.* 255, 26–36. <http://dx.doi.org/10.1016/j.enggeo.2019.04.013>, URL: <https://www.sciencedirect.com/science/article/pii/S001379521831915X>.
- Jameson, A., Schmidt, W., Turkel, E., 1981. Numerical solution of the Euler equations by finite volume methods using Runge–Kutta time stepping schemes. In: AIAA 14th Fluid and Plasma Dynamic Conference. <http://dx.doi.org/10.2514/6.1981-1259>.
- JMA, 2021. Japan Meteorology Agency website. URL: <https://www.jma.go.jp/jma/indexe.html>.
- JSECE, 2016. Investigation report on the landslide disasters caused by the 2016 Kumamoto earthquake (free translation from Japanese). *Jpn. Soc. Eros. Control Eng.* URL: [http://www.jsece.or.jp/archive/survey/20160421/20161213\\_workshop.pdf](http://www.jsece.or.jp/archive/survey/20160421/20161213_workshop.pdf).
- Khayyer, A., Gotoh, H., Falahat, H., Shimizu, Y., 2018. An enhanced ISPH–SPH coupled method for simulation of incompressible fluid–elastic structure interactions. *Comput. Phys. Comm.* 232, 139–164. <http://dx.doi.org/10.1016/j.cpc.2018.05.012>.
- Koshizuka, S., Oka, Y., 1996. Moving-particle semi-implicit method for fragmentation of incompressible fluid. *Nucl. Sci. Eng.* 123, 421–434. <http://dx.doi.org/10.13189/NSE96-A24205>.
- Kumar, K., Soga, K., Delenne, J.-Y., 2012. Granular flows in fluid. In: Discrete Element Modelling of Particulate Media. The Royal Society of Chemistry, pp. 59–66. <http://dx.doi.org/10.1039/9781849735032-00059>.
- Laloui, L., Eichenberger, J., Nuth, M., 2013. Modeling landslides in partially saturated slopes subjected to rainfall infiltration. *Mech. Unsaturated Geomater.* <http://dx.doi.org/10.1002/9781118616871.ch10>.
- Lee, C.H., Gil, A.J., Greto, G., Kulasegaram, S., Bonet, J., 2016. A new Jameson–Schmidt–Turkel smooth particle hydrodynamics algorithm for large strain explicit fast dynamics. *Comput. Methods Appl. Mech. Engrg.* 311, 71–111. <http://dx.doi.org/10.1016/j.cma.2016.07.033>.
- Liang, Y., Chandra, B., Soga, K., 2022. Shear band evolution and post-failure simulation by the extended material point method (XMPM) with localization detection and frictional self-contact. *Comput. Methods Appl. Mech. Engrg.* 390, 114530. <http://dx.doi.org/10.1016/j.cma.2021.114530>.
- Liberky, L., Petschek, A., 1990. Smooth particle hydrodynamics with strength of materials. In: Advances in the Free-Lagrange Method. Trease and Crowkey, pp. 248–257. [http://dx.doi.org/10.1007/3-540-54960-9\\_58](http://dx.doi.org/10.1007/3-540-54960-9_58).
- Lin, C., Pastor, M., Li, T., Liu, X., Lin, C., Qi, H., Sheng, T., 2019. A PFE/IE–SPH joint approach to model landslides from initiation to propagation. *Comput. Geotech.* 114, 103153. <http://dx.doi.org/10.1016/j.compgeo.2019.103153>.

- Lucy, L., 1977. A numerical approach to the testing of the fission hypothesis. *Astron. J.* 82, 1013–1024. <http://dx.doi.org/10.1086/112164>.
- Maeda, K., Sakai, H., Sakai, M., 2004. Development of seepage failure analysis method of ground with smoothed particle hydrodynamics (in Japanese). *J. Appl. Mech.* 7, 775–786.
- Maeda, K., Sakai, H., Sakai, M., 2006. Development of seepage failure analysis method of ground with smoothed particle hydrodynamics. *Struct. Eng./Earthq. Eng.* 23 (2), 307–319. <http://dx.doi.org/10.2208/jcsesee.23.307s>.
- McDougall, S., Hungr, O., 2004. A model for the analysis of rapid landslide motion across three-dimensional terrain. *Can. Geotech. J.* 41 (6), 1084–1097. <http://dx.doi.org/10.1139/t04-052>.
- Monaghan, J., 1992. Smoothed particle hydrodynamics. *Annu. Rev. Astron. Astrophys.* 30, 543–574. <http://dx.doi.org/10.1146/annurev.aa.30.090192.002551>.
- Montgomery, C., 2014. *Environmental Geology*, tenth ed. McGraw-Hill.
- Morikawa, D., Asai, M., 2021. Coupling total Lagrangian SPH-EISPH for fluid-structure interaction with large deformed hyperelastic solid bodies. *Comput. Methods Appl. Mech. Engrg.* 381, <http://dx.doi.org/10.1016/j.cma.2021.113832>.
- Morikawa, D., Asai, M., 2022. Soil-water strong coupled ISPH based on u-w-p formulation for large deformation problems. *Comput. Geotech.* 142, <http://dx.doi.org/10.1016/j.compgeo.2021.104570>.
- Morikawa, D., Asai, M., Idris, N., Imoto, Y., Isshiki, M., 2019. Improvements in highly viscous fluid simulation using a fully implicit SPH method. *Comput. Part. Mech.* 6, 529–544. <http://dx.doi.org/10.1007/s40571-019-00231-6>.
- Morris, J., Fox, P., Zhu, Y., 1997. Modeling low Reynolds number incompressible flows using SPH. *J. Comput. Phys.* 136 (1), 214–226. <http://dx.doi.org/10.1006/jcph.1997.5776>.
- Naili, M., Matsushima, T., 2005. A 2D smoothed particle hydrodynamics method for liquefaction induced lateral spreading analysis. *J. Appl. Mech.* 8, 591–599. <http://dx.doi.org/10.2208/journalam.8.591>.
- Pastor, M., Blanc, T., Drempetic, V., Dutto, P., Stickle, M.M., Yague, A., 2015. Modelling of landslides: and SPH approach. *CMES* 109–110 (2), 183–220. <http://dx.doi.org/10.3970/cmes.2015.109.183>.
- Pastor, M., Blanc, T., Pastor, M., 2009. A depth-integrated viscoplastic model for dilatant saturated cohesive-frictional fluidized mixtures: application to fast catastrophic landslides. *J. Non-Newton. Fluid.* 158, 142–153. <http://dx.doi.org/10.1016/j.jnnfm.2008.07.014>.
- Peng, X., Yu, P., Chen, G., Xia, M., Zhang, Y., 2019. Development of a coupled DDA-SPH method and its application to dynamic simulation of landslides involving solid-fluid interaction. *Rock Mech. Rock Eng.* 53, 113–131. <http://dx.doi.org/10.1007/s00603-019-01900-x>.
- Pereira, G., Cleary, P., Lemiale, V., 2017. SPH method applied to compression of solid materials for a variety of loading conditions. *Appl. Math.* 44, 72–90. <http://dx.doi.org/10.1016/j.apm.2016.12.009>.
- Putra, O., 2020. Evaluation of Shear Strength Characteristics of Unsaturated Undisturbed Volcanic Ash Soil Subjected to Static and Cyclic Loading for Slope Stability Analysis (Ph.D. thesis). Kyushu University.
- Randles, P., Libersky, L., 1996. Smoothed particle hydrodynamics: some recent improvements and applications. *Comput. Methods Appl. Mech. Engrg.* 139, 375–408. [http://dx.doi.org/10.1016/S0045-7825\(96\)01090-0](http://dx.doi.org/10.1016/S0045-7825(96)01090-0).
- Salimzadeh, S., Khalili, N., 2015. A three-phase XFEM model for hydraulic fracturing with cohesive crack propagation. *Comput. Geotech.* 69, 82–92. <http://dx.doi.org/10.1016/j.compgeo.2015.05.001>.
- Sanborn, S., Prévost, J., 2011. Frictional slip plane growth by localization detection and extended finite element method (XFEM). *Int. J. Numer. Anal. Methods Geomech.* 35 (11), 1278–1298. <http://dx.doi.org/10.1002/nag.958>.
- Schoenberg, I., 1964. Spline interpolation and best quadrature formulae. *Bull. Amer. Math. Soc.* 70 (1), 143–148. <http://dx.doi.org/10.1090/S0002-9904-1964-11054-5>.
- Schofield, A., Wroth, C., 1968. *Critical State Soil Mechanics*.
- Soga, K., Alonso, E., Yerro, A., Kumar, K., Bandara, S., 2015. Trends in large-deformation analysis of landslide mass movements with particular emphasis on the material point method. *Geotechnique* 66, 248–273. <http://dx.doi.org/10.1680/jgeot.15.LM.005>.
- Stellingwerf, R., Wingate, C., 1993. Impact modeling with smooth particle hydrodynamics. *Int. J. Impact Engng.* 14, 707–718. [http://dx.doi.org/10.1016/0734-743X\(93\)90065-F](http://dx.doi.org/10.1016/0734-743X(93)90065-F).
- Terzaghi, K., 1950. Mechanism of Landslides. application of Geology to Engineering Practice. Harvard University, Cambridge, Mass, <http://dx.doi.org/10.1130/Berkey.1950.83>.
- Tsuji, T., Nakamura, K., Yabumoto, K., Tanaka, T., 2007. Large-scale DEM-CFD coupling simulation. *J. Soc. Powder Technol. Jpn* 44 (3), 173–179. <http://dx.doi.org/10.4164/sptj.44.173>.
- Violeau, D., Issa, R., 2007. Numerical modelling of complex turbulent free-surface flows with the SPH method: An overview. *Internat. J. Numer. Methods Fluids* 53, 277–304. <http://dx.doi.org/10.1002/fld.1292>.
- Wang, W., Chen, G., Han, Z., Zhou, H., Jing, P., 2016a. 3D numerical simulation of debris-flow motion using SPH method incorporating non-Newtonian fluid behavior. *Nat. Hazards* 81, 1981–1998. <http://dx.doi.org/10.1007/s11069-016-2171-x>.
- Wang, W., CHEN, G.-q., ZHANG, H., Zhang, Y., Zheng, L., 2017. Dynamic simulation of landslide dam behavior considering kinematic characteristics using a coupled DDA-SPH method. *Eng. Anal. Bound. Elem.* 80, 172–183. <http://dx.doi.org/10.1016/j.enganabound.2017.02.016>.
- Wang, W., Chen, G., Zhang, H., Zhou, S., Liu, S., Wu, Y., Fan, F., 2016b. Analysis of landslide-generated impulsive waves using a coupled DDA-SPH method. *Eng. Anal. Bound. Elem.* 64, 267–277. <http://dx.doi.org/10.1016/j.enganabound.2015.12.014>.
- Wang, L., Xu, F., Yang, Y., 2021. An improved total Lagrangian SPH method for modeling solid deformation and damage. *Eng. Anal. Bound. Elem.* 133, 286–302. <http://dx.doi.org/10.1016/j.enganabound.2021.09.010>.
- Wang, W., Yin, K., Chen, G., Chai, B., Han, Z., Zhou, J., 2019. Practical application of the coupled DDA-SPH method in dynamic modeling for the formation of landslide dam. *Landslides* 16, 1021–1032. <http://dx.doi.org/10.1007/s10346-019-01143-5>.
- Zhao, S., Bui, H., Lemiale, V., Nguyen, G., Darve, F., 2018. A generic approach to modelling flexible confined boundary conditions in SPH and its application. *Int. J. Numer. Anal. Methods Geomech.* 43, 1005–1031. <http://dx.doi.org/10.1002/nag.2918>.
- Zienkiewicz, O., Chan, A., Pastor, M., Schrefler, B., Shiomi, T., 1999. *Computational Geomechanics with Special Reference to Earthquake Engineering*. John Wiley & Sons, Ltd.